

**Key Points:**

- The central South-Pole Aitken basin compositional anomaly is formed of cryptomare deposits rather than a differentiated impact melt sheet
- South-Pole Aitken basin resembles other lunar basins having mare/cryptomare infilling the center, adding 0.5%–1.8% to the global basalt inventory
- Crustal thickness variations may account for the concentration of farside maria in the South-Pole Aitken basin, yet it remains underfilled

**Supporting Information:**

Supporting Information may be found in the online version of this article.

**Correspondence to:**

J. W. Head and J. Liu,  
James\_Head@brown.edu;  
liuji@nao.cas.cn

**Citation:**

Wang, X., Head, J. W., Chen, Y., Zhao, F., Kreslavsky, M. A., Wilson, L., et al. (2024). Lunar farside South Pole-Aitken basin interior: Evidence for more extensive central cryptomaria in the South Pole-Aitken compositional anomaly (SPACA). *Journal of Geophysical Research: Planets*, 129, e2023JE008176. <https://doi.org/10.1029/2023JE008176>

Received 24 OCT 2023

Accepted 29 APR 2024

**Author Contributions:**

**Conceptualization:** Xing Wang, James W. Head

**Funding acquisition:** Jianjun Liu

**Investigation:** Xing Wang, Yuan Chen, Feiyue Zhao








**Methodology:** Xing Wang, Yuan Chen, Feiyue Zhao, Yuqi Qian

**Supervision:** James W. Head, Jianjun Liu, Chunlai Li

© 2024. The Authors.

This is an open access article under the terms of the [Creative Commons Attribution-NonCommercial-NoDerivs License](#), which permits use and distribution in any medium, provided the original work is properly cited, the use is non-commercial and no modifications or adaptations are made.

## Lunar Farside South Pole-Aitken Basin Interior: Evidence for More Extensive Central Cryptomaria in the South Pole-Aitken Compositional Anomaly (SPACA)

Xing Wang<sup>1,2,3</sup> , James W. Head<sup>3</sup> , Yuan Chen<sup>1</sup> , Feiyue Zhao<sup>4</sup>, Mikhail A. Kreslavsky<sup>5</sup> , Lionel Wilson<sup>6</sup> , Yuqi Qian<sup>7</sup> , Jianjun Liu<sup>1,2</sup>, and Chunlai Li<sup>1,2</sup> 

<sup>1</sup>Key Laboratory of Lunar and Deep Space Exploration, National Astronomical Observatories, Chinese Academy of Sciences, Beijing, China, <sup>2</sup>School of Astronomy and Space Science, University of Chinese Academy of Sciences, Beijing, China, <sup>3</sup>Department of Earth, Environmental, and Planetary Sciences, Brown University, Providence, RI, USA, <sup>4</sup>Beijing Planetarium, Beijing, China, <sup>5</sup>Earth and Planetary Sciences, University of California, Santa Cruz, CA, USA, <sup>6</sup>Lancaster Environment Centre, Lancaster University, Lancaster, UK, <sup>7</sup>Department of Earth Sciences, University of Hong Kong, Hong Kong, China

**Abstract** In the central area of the South Pole-Aitken (SPA) basin, an intermediate albedo, mafic compositional anomaly (SPA Compositional Anomaly, SPACA) has been documented by previous studies, but its origin remains uncertain. We conducted an investigation of stratigraphic units defined based on morphology and composition and their relative ages, and placed these in the context of basin topography and the observed sequence of geological events, all helping to distinguish between SPACA origins from: (a) SPA impact melt, (b) volcanism induced by the SPA event and (c) lunar cryptomaria. We conclude that SPACA represents extensive traditional cryptomare deposits overlying the SPA impact melt. We interpret the basin center to be filled with cryptomare deposits at least one km thick ( $>1 \times 10^5 \text{ km}^3$  in volume) with ages not younger than Early Imbrian. We attribute the relatively high albedo of SPACA to lateral mixing of ejecta from nearby highlands craters and basins, and conclude that the cryptomaria basalts are likely to be very similar to basalts on the nearside. Our findings imply a 0.5%–1.8% increase in the total volume of global lunar mare and cryptomare deposits. These results show that mare volcanism was common only in areas of thinnest crust on the lunar farside, a factor important in understanding lunar nearside-farside asymmetries. Despite this significant increase in total cryptomare volume in the SPA basin center, SPA remains underfilled relative to nearside mascon basins. Return of mare basalts from the SPA region by Chang'E-6 will help determine potential mantle source region differences and petrogenetic pathways.

**Plain Language Summary** On the enigmatic farside of the Moon, a huge impact basin called SPA basin occupies an immense area (~2,500 km diameter). Previous spectroscopic investigations identified four compositional zones across SPA, and the central one shows a distinctive high-Ca pyroxene anomaly, designated the “South Pole-Aitken compositional anomaly” (SPACA). SPACA has a higher albedo compared to typical maria but lower than lunar highlands and has a paucity of impact craters relative to other SPA units. Previous studies concluded that SPACA is either associated with (1) the SPA impact melt sheet or (2) subsequent volcanic resurfacing events of a special composition induced by the SPA impact. Our reassessment favors the hypothesis that SPACA represents cryptomaria erupted into the basin center during a period of higher impact flux, resulting in lateral dusting of the dark mare surfaces by highland material, thereby raising their albedos. Consequently, the SPACA is similar to other lunar basins in that cryptomaria were deposited in the basin center, followed by maria when the impact flux declined and lateral dusting was minimal. Our SPA cryptomare volume estimates represent a 0.5%–1.8% increase in the total volume of global lunar mare and cryptomare deposits, but SPA remains underfilled relative to nearside giant basins.

### 1. Introduction

Among the several documented differences between the lunar nearside and farside (crustal thickness, composition, etc.), the striking difference in the areal distribution and abundance of mare basalts (Figures 1a and 1b) has been a mystery since discovered by Luna 3 in 1959 (Barabashov, 1961). There is a distinct paucity of mare deposits on the lunar farside in both areal coverage and volume, and it became clear early on that most farside maria are concentrated within the South Pole-Aitken (SPA) basin (Figure 1b) (e.g., Head, 1976; Pasckert

**Validation:** James W. Head, Yuan Chen, Mikhail A. Kreslavsky, Lionel Wilson, Jianjun Liu, Chunlai Li  
**Writing – original draft:** Xing Wang  
**Writing – review & editing:** James W. Head, Mikhail A. Kreslavsky, Lionel Wilson

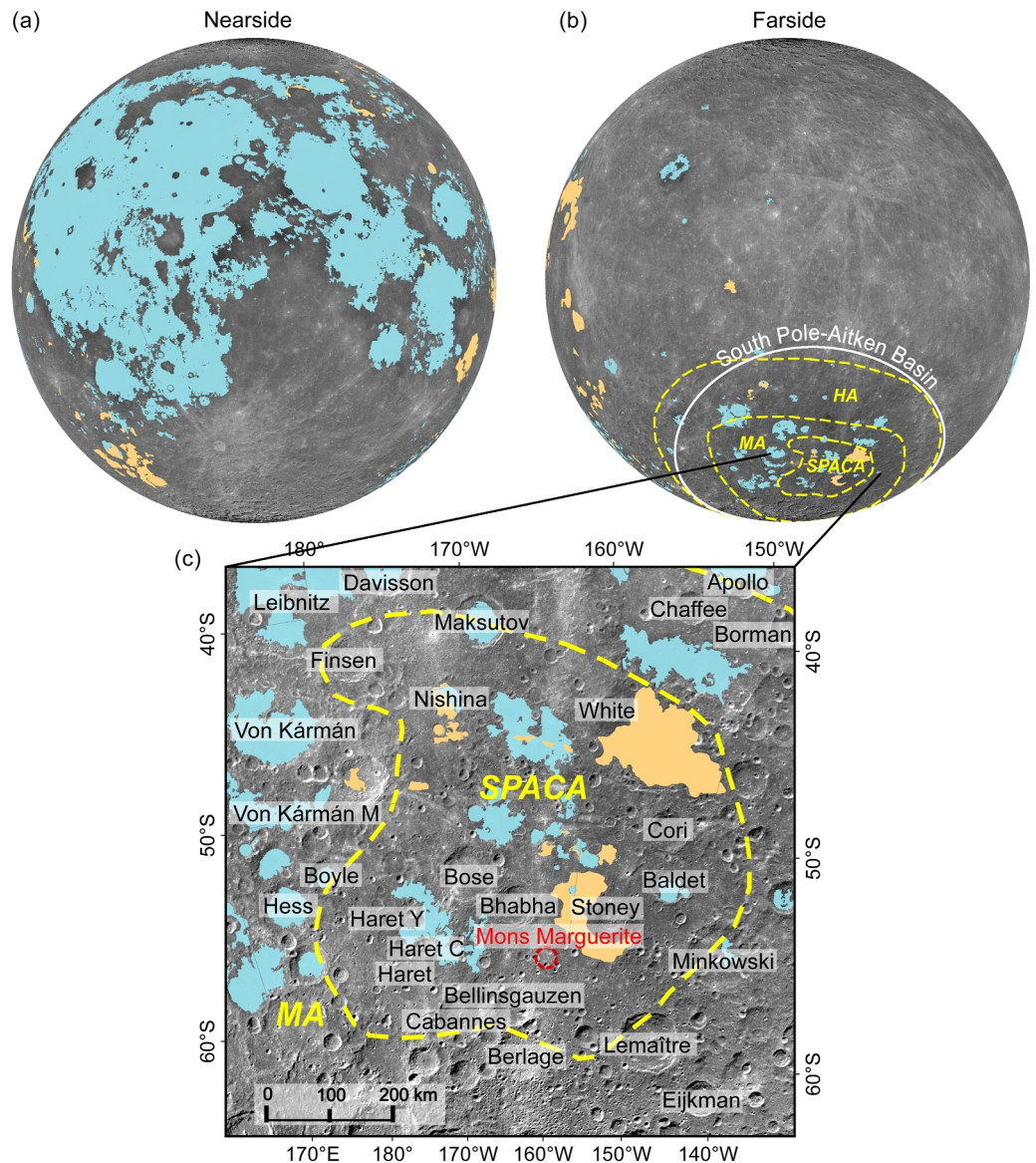


**Figure 1.** Global mare and cryptomare distribution and the location of the SPACA. (a, b) display the asymmetric mare distribution between lunar nearside and farside. The mare boundaries are from Nelson et al. (2014). The cryptomare boundaries were obtained by Whitten and Head (2015a, 2015b). The yellow dashed lines in panel (b) outline the compositional zones within the South Pole-Aitken (SPA) basin (Moriarty & Pieters, 2018). SPACA = SPA Compositional Anomaly; MA = Mg-pyroxene Annulus; HA = Heterogeneous Annulus. (c) is a zoomed-in image of the SPACA, and the location of Mons Marguerite is marked by a cyan circle. The background image is Chang'E-2 digital orthophoto model. (a, b) are in orthographic projection. (c) and all other figures in this paper (unless otherwise specified) are in stereographic projection centered at the center of SPA (191.1°E, 53.2°S; Garrick-Bethell & Zuber, 2009).

et al., 2018; Pieters et al., 2001; Yingst & Head, 1997, 1999), the largest and oldest confirmed impact basin on the Moon (e.g., Petro & Pieters, 2004; Spudis et al., 1994). However, the thickness and total volume of these identified farside mare deposits are clearly much smaller than that on the lunar nearside. As observed in the circular nearside mare-filled impact basins (e.g., Imbrium, Serenitatis and Crisium), regional mare fill typically occurs in the basin centers, in contrast to the series of relatively small mare patches present in the SPA basin center (Pasckert et al., 2018; Yingst & Head, 1997, 1999).

It is well-known that the earliest mare deposits often occur as cryptomaria, which were named by Head and Wilson (1992). Cryptomaria are the mare basalt plains that have been dusted or covered with higher albedo

highland impact crater and basin ejecta and are detected primarily through dark-halo craters (DHCs) that penetrate through the cover and excavate low-albedo mare material (Antonenko et al., 1995; Head & Wilson, 1992; Schultz & Spudis, 1983; Whitten & Head, 2015a). Is it possible that there are more extensive mare deposits in the SPA basin center but in the form of buried cryptomaria that have not yet been recognized?

Moriarty and Pieters (2018) mapped the SPA basin into four compositional zones based on their spectral features (Figure 1b). The SPA central zone is designated the “South Pole-Aitken compositional anomaly” (SPACA) (Figure 1c), and is characterized by a distinctive intermediate-Ca, Fe pyroxene-bearing surface composition. The SPACA is surrounded outward by the “Mg-pyroxene Annulus”, which is dominated by Mg-pyroxene. Further outward from the SPA center is the “Heterogeneous Annulus”, characterized as localized Mg-pyroxene mixed with feldspathic materials. Finally, the most distant from the center is the predominantly feldspathic “SPA exterior”. The SPA areally centered SPACA unit is also primarily distributed in the topographically low-lying center of the SPA. Although the SPACA is characterized by a potential basaltic composition, it has an intermediate-high albedo brighter than typical mares but lower than the surrounding Mg-pyroxene Annulus (Moriarty & Pieters, 2018).

A layer similar in composition to the Mg-pyroxene Annulus is also noted underlying the SPACA region, as the central peaks of several craters within this region exhibit Mg-pyroxene signatures (Moriarty et al., 2021a; Moriarty & Pieters, 2018). The thorium (Th) abundance (Lawrence et al., 2003) across the SPACA is relatively lower than in the surroundings, and the observed abundance is probably a result of impact cratering excavation and redistribution from surrounding units (Moriarty et al., 2021a). Head et al. (2010) also discovered that the SPA basin center is deficient in craters relative to surrounding heavily cratered lunar terrains, further suggesting interior resurfacing processes.

On the basis of all these characteristics, the SPACA is currently interpreted as either (a) volcanic resurfacing deposits, with a mineralogy distinct from typical mare basalts (Moriarty et al., 2021a; Moriarty et al., 2022, 2022) or (b) a differentiated SPA impact melt sheet (Ohtake et al., 2014; Uemoto et al., 2017). Moriarty et al. (2021a, 2021b, 2022) suggest that there are at least three types of volcanic deposits occurring within the SPACA: (a) younger mare basalts, (b) cryptomaria, with a composition distinctive from the later SPA and nearside mare basalts, and (c) Mons Marguerite Mafic Magmas ( $M^4$ ). Mons Marguerite (the informal name of Mafic Mound which is used in Moriarty et al., 2021a, 2021b, 2022) is a distinctive circular structure located in the southern part of SPACA (Figure 1c). On the basis of its distinctive homogeneous high-Ca pyroxene (HCP)-bearing composition, positive topography and higher albedo, Moriarty and Pieters (2015) interpreted it as a volcanic construct associated with an unusual type of non-mare volcanism that resulted from mantle melting related to the gigantic SPA basin impact. Other researchers favor interpreting the SPACA HCP composition that occurs in the SPA center as a differentiated SPA impact melt sheet (Ohtake et al., 2014; Uemoto et al., 2017). These workers further hypothesize that the thickness of such an HCP-bearing *upper* differentiated impact melt sheet could reach up to  $\sim 7$  km, overlying a  $>8$  km thick low-Ca pyroxene (LCP)-bearing *lower* impact melt sheet.

Several studies have been conducted to investigate the possible presence of cryptomare in the SPA basin center. To explain the paucity of large craters documented by Head et al. (2010), Whitten and Head (2013) applied a volcanic flooding simulation to the SPA topography and concluded that  $\sim 1$ – $2$  km thickness of cryptomaria could account for the paucity of craters in the basin center. The global cryptomare investigation by Whitten and Head (2015a, 2015b) outlined several candidate cryptomaria in the SPA center (Figure 1c) with a total area of  $2.96 \times 10^4$  km<sup>2</sup>, corresponding to a total volume of  $4.43 \times 10^4$  km<sup>3</sup>. Chuang et al. (2022) attempted to use surface roughness to distinguish the cryptomare from other volcanic units in the SPA basin center, but they pointed out that using surface roughness alone may not be sufficient to do that. The result of the global cryptomare identification using the Gravity Recovery and Interior Laboratory (GRAIL) gravity data by Izquierdo et al. (2024) also shows the possibility of a wider distribution of cryptomaria in the entire SPA basin, including the basin center.

In summary, the origin of the SPACA remains uncertain: (a) a differentiated impact melt sheet, (b) mare volcanism in the form of cryptomaria, or (c) a unique type of intermediate-albedo basalt related to farside mantle melting induced by the anomalously large SPA basin-forming event. In this analysis, we perform a more detailed investigation on the nature of the SPACA region, place it in the context of the observed stratigraphic and geologic sequence of events, and reassess the theories for its origin. We test the differentiated impact melt hypothesis for SPACA from the perspective of the potential scale of the SPA impact melt sheet (Melosh et al., 2017; Potter et al., 2012).



Our analysis leads us to favor the hypothesis that a significant part of the SPACA terrain likely represents more extensive cryptomaria deposits than previously estimated. We interpret the apparent intrinsic albedo difference from mare basalts to be largely due to dusting and regolith mixing with highland materials delivered by younger craters or basins within and near the SPACA. Our findings also result in a significant increase in the total volume of farside mare and cryptomare basalts, and we place this in the context of the global lunar mare and cryptomare deposit volume, and investigate implications for the nearside-farside asymmetry in mare basalt deposits on the Moon.

## 2. Data and Methods

### 2.1. Data Sets

Multiple data sets and sources were employed to identify and map the SPACA and adjacent deposits in central SPA. Digital elevation models (DEM) (Figure 2b) and slope data (Figure 2d) derived from combined Lunar Orbiter Laser Altimeter (LOLA) data and Selenological and Engineering Explorer (SELENE or Kaguya) data (SLDEM2015, Barker et al., 2016) provide the basic topographic information for the SPACA. The LOLA-derived surface roughness map is used to compare with other lunar cryptomaria in morphology (Figure 2i) (Kreslavsky et al., 2013). We obtain mineralogical and compositional characteristics from Chandrayaan-1 Moon Mineralogy Mapper ( $M^3$ ) hyperspectral data (Pieters et al., 2009) and Kaguya Multiband Image (MI) multispectral data (Ohtake et al., 2008). MI data with high resolution provide more spatial information and  $M^3$  data with far more spectral bands provide more spectral information. In this work, both data sets are validated against each other, especially at high latitudes ( $>50^\circ$ ) where MI data become less accurate (Lemelin et al., 2015). We generate a pyroxene composition map (described in Section 2.2; Figure 2e, Figure S1 in Supporting Information S1), optical maturity (OMAT; Figure 2g; Lemelin et al., 2019), and FeO abundance map (Figure 2f; Lemelin et al., 2015) from MI data. For  $M^3$  data, we focus more on the spectral characterization. Most  $M^3$  spectral data used in this study were collected from  $M^3$  optical period 2C2 (OP2C2) as it provides the broadest coverage of SPACA. In the few areas without OP2C2 coverage, we supplement it with OP2C1 data. Th and FeO abundance maps, derived from Lunar Prospector gamma ray spectrometer data (LP GRS) (Lawrence et al., 2002, 2003), are also employed for compositional analysis (Figures 4a and 4b). The LOLA albedo map (Figure 2h) (Lemelin et al., 2016) and the  $M^3$  1,489 nm band are used to assess the variation in albedo. Crustal thickness maps are obtained from GRAIL (Zuber et al., 2013) derived data (Wieczorek et al., 2013) (Figure 2c). The crater information used in this work is from the Povilaitis et al. (2018) for craters 5–20 km in diameter, and Head et al. (2010) for craters  $>20$  km in diameter. All the data above are overlain on the Chang'E-2 digital orthophoto model (DOM) image (Li et al., 2018) for presentation. All original data are available in the NASA Planetary Data System (PDS) except the CE-2 DOM image that can be accessed at China's Lunar and Planetary Data Release System (<https://moon.bao.ac.cn/>). In addition, the new geological maps of the northern portion and the whole SPA basin (Ivanov et al., 2018; Poehler et al., 2020) are adopted in this work to clarify stratigraphic relationships between different units.

### 2.2. Spectral Data Processing

Given their higher-resolution and better data quality compared with  $M^3$  data within the SPACA, Kaguya MI multispectral data are used to generate the map revealing the variations in pyroxene composition in the study area. The original sampling of MI data is 2,048 pixels per degree (ppd) ( $\sim 15$  m/pixel); we resampled them to 128 ppd (237 m/pixel) to reduce the computation. This resolution is still sufficient for our large-scale analysis. MI data have a total of 8 spectral bands (415, 750, 900, 950, 1,000, 1,050, 1,250, and 1,550 nm wavelength), and we can obtain the pyroxene composition using the diagnostic absorption features around 1  $\mu\text{m}$ . However, due to the limited band number, we cannot determine the exact band center, but we can access the relative variation of the band centers using band tilt that has been applied to the MI data (e.g., Uemoto et al., 2017) and Clementine data (Pieters et al., 2001). The straight lines connecting the reflectance values between 750 and 1,550 nm are taken as the spectral continuum, and each reflectance spectrum is divided by its continuum to obtain the continuum-removed spectrum. The band tilt can then be measured by the difference in the continuum-removed reflectance at 900 and 1,000 nm (Figure S2 in Supporting Information S1), which can reflect the pyroxene composition (Figure S1 in Supporting Information S1). An upward 900–1,000 nm band tilt indicates that the band center is below 950 nm (namely the value  $\leq 0$  in Figure S1 in Supporting Information S1), which can be classified as LCP, and conversely, a downward 900–1,000 nm band tilt (namely the value  $> 0$  in Figure S1 in Supporting Information S1) suggests the presence of HCP.



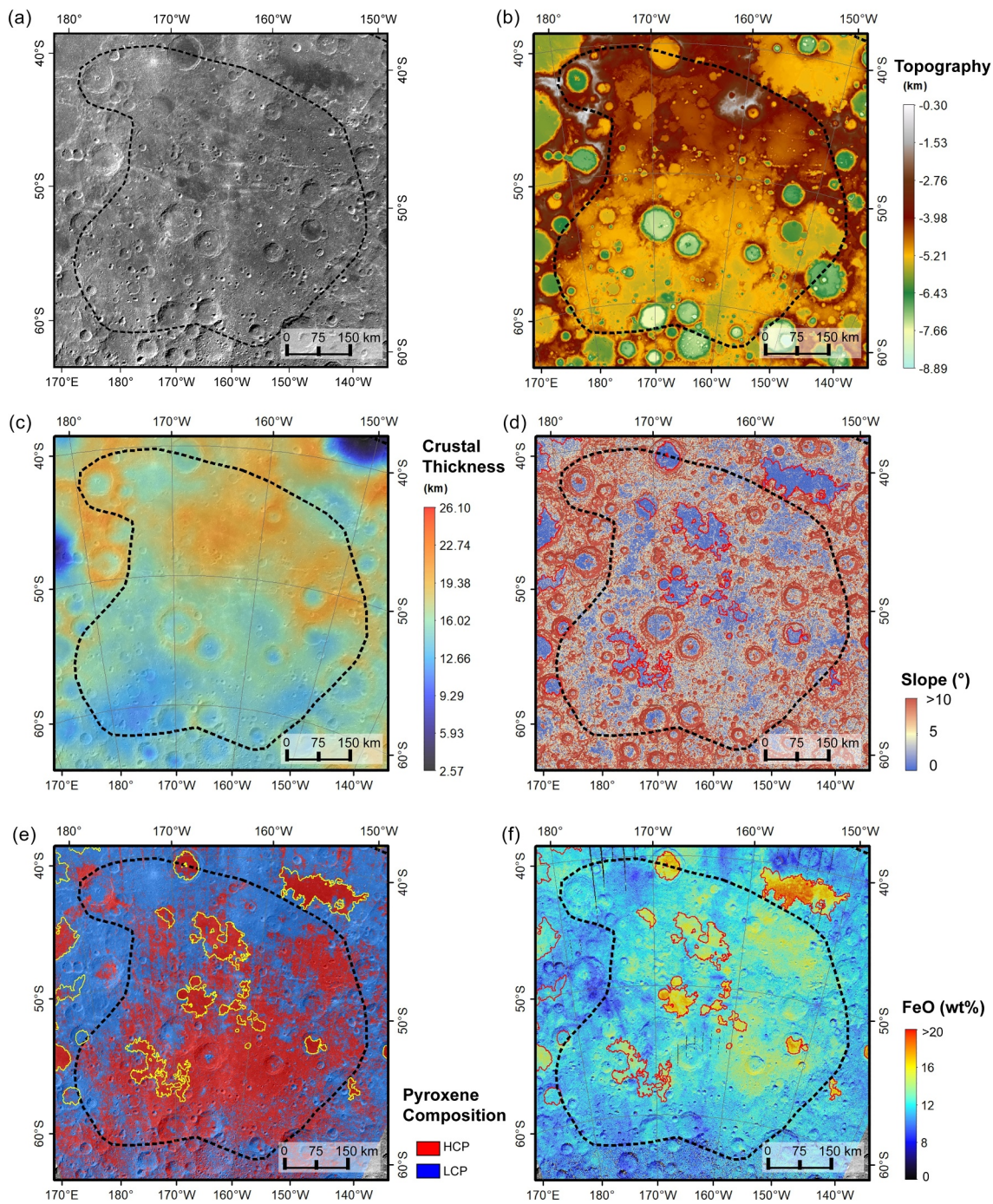


**Figure 2.** Basic characteristics of the SPACA. (a) CE-2 digital orthophoto model image (Li et al., 2018). (b) Topographic map from SLDEM (Barker et al., 2016). An obvious north-south difference in elevation can be observed. (c) Crustal thickness derived from Gravity Recovery and Interior Laboratory data (Wieczorek et al., 2013). The north-south difference appears to be associated with surface topography. (d) Surface slope map derived from SLDEM (Barker et al., 2016). Many areas within the SPACA show relatively lower slopes ( $<5^\circ$ ). (e) Pyroxene composition map obtained from Kaguya MI data; the method can be found in Section 2.2. (f) Iron abundance map calculated from Kaguya MI data (Lemelin et al., 2015). (g) OMAT map obtained from Kaguya MI data (Lemelin et al., 2019). The ejecta from the Finsen and Alder craters may contribute to the albedo increase in the western part of the SPACA. Several long, bright, ray-like north-south ejecta deposits across the SPACA can also be observed, which can be traced back to Jackson crater. (h) Lunar Orbiter Laser Altimeter albedo map (Lemelin et al., 2016). Some areas outside the younger maria within the SPACA also show relatively low albedo. (i) Surface roughness for 1.84 km baseline (Kreslavsky et al., 2013). Some areas outside the younger maria within the SPACA also show relatively low surface roughness. (j) Crater densities of SPACA for craters  $\geq 5$  km in diameter, calculated in neighborhoods of radius 50 km. In panels (d–j), the mare boundaries are marked in red or yellow (Nelson et al., 2014).



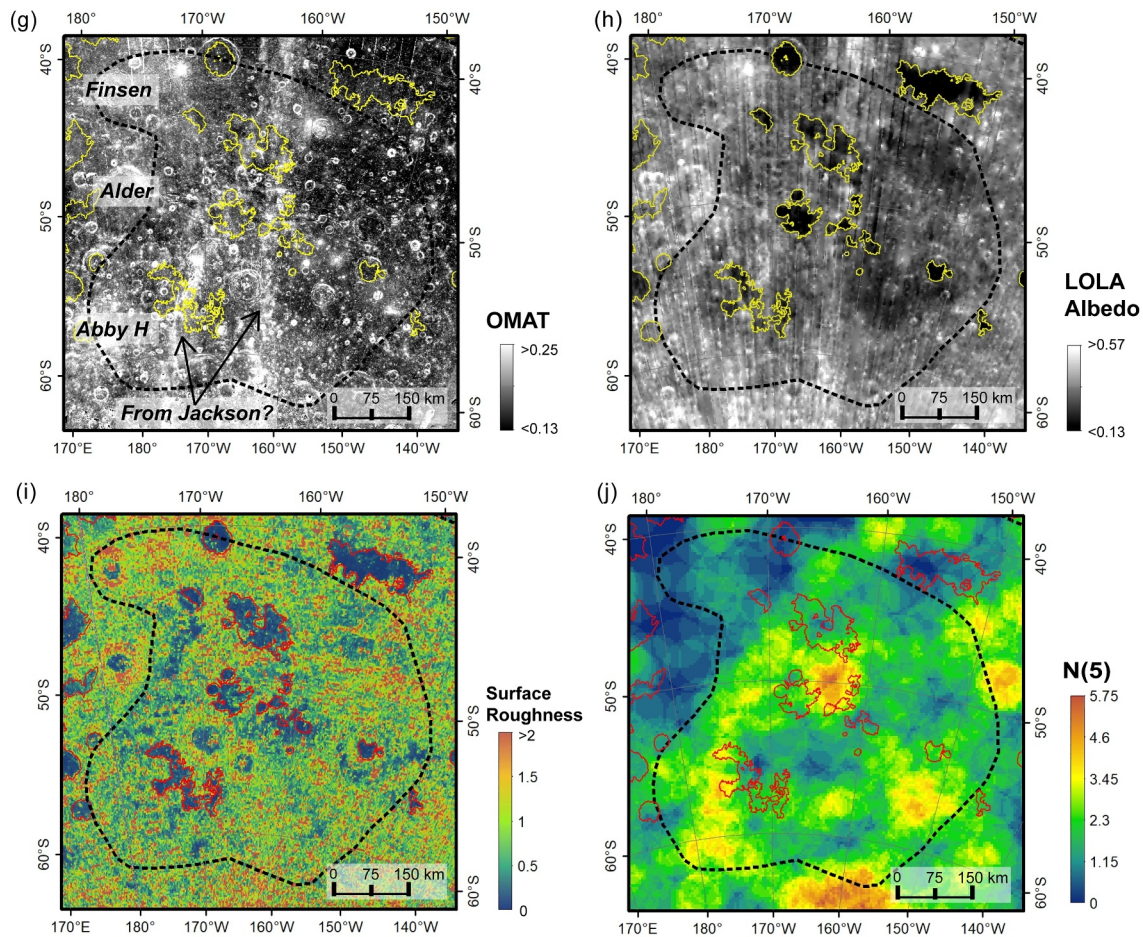


Figure 2. (Continued)

For the  $M^3$  data, we only focus on the spectra from fresh craters that show relatively deep band absorptions. For minimizing thermal effects, only wavelengths shorter than 2,500 nm are used in this work. All collected spectra are smoothed using the Savitzky-Golay methods (Savitzky & Golay, 1964) to reduce the influence of noise. Then, the two-straight-line method is adopted to remove the spectral continuum (Liu et al., 2022; Zhang et al., 2016). The two straight lines represent the tangents of the absorption band connecting the left and right shoulders. For 1  $\mu\text{m}$  absorption, the left and right tangent points can be found within the ranges of 600–800 nm and 1,300–1,800 nm, respectively. One point was taken in each of these two ranges iteratively until the line joining the two points completely covers the 1  $\mu\text{m}$  absorption band, and this straight line is treated as the tangent line of the 1  $\mu\text{m}$  band. The tangent line of the 2  $\mu\text{m}$  band can be obtained in the same way. Fourth order polynomials are used to fit the continuum-removed spectrum around the 1 and 2  $\mu\text{m}$  absorptions, and we consider the wavelengths corresponding to the minima of the fitted lines as the band centers. It should be mentioned that in most cases in this work HCP often refers to the pyroxene with intermediate-Ca and Fe, but we call it HCP in order to distinguish it from LCP.

### 3. The Origin of SPACA

#### 3.1. Reconsidering the SPA Structure and the Differentiated SPA Impact Melt Sheet Origin

As mentioned above, several previous studies have interpreted the SPACA compositional anomaly in the central SPA basin as being due to the occurrence of a differentiated SPA impact melt sheet (Ohtake et al., 2014; Uemoto et al., 2017; see also Vaughan & Head, 2014; Hurwitz & Kring, 2014). We here reconsider the differentiated

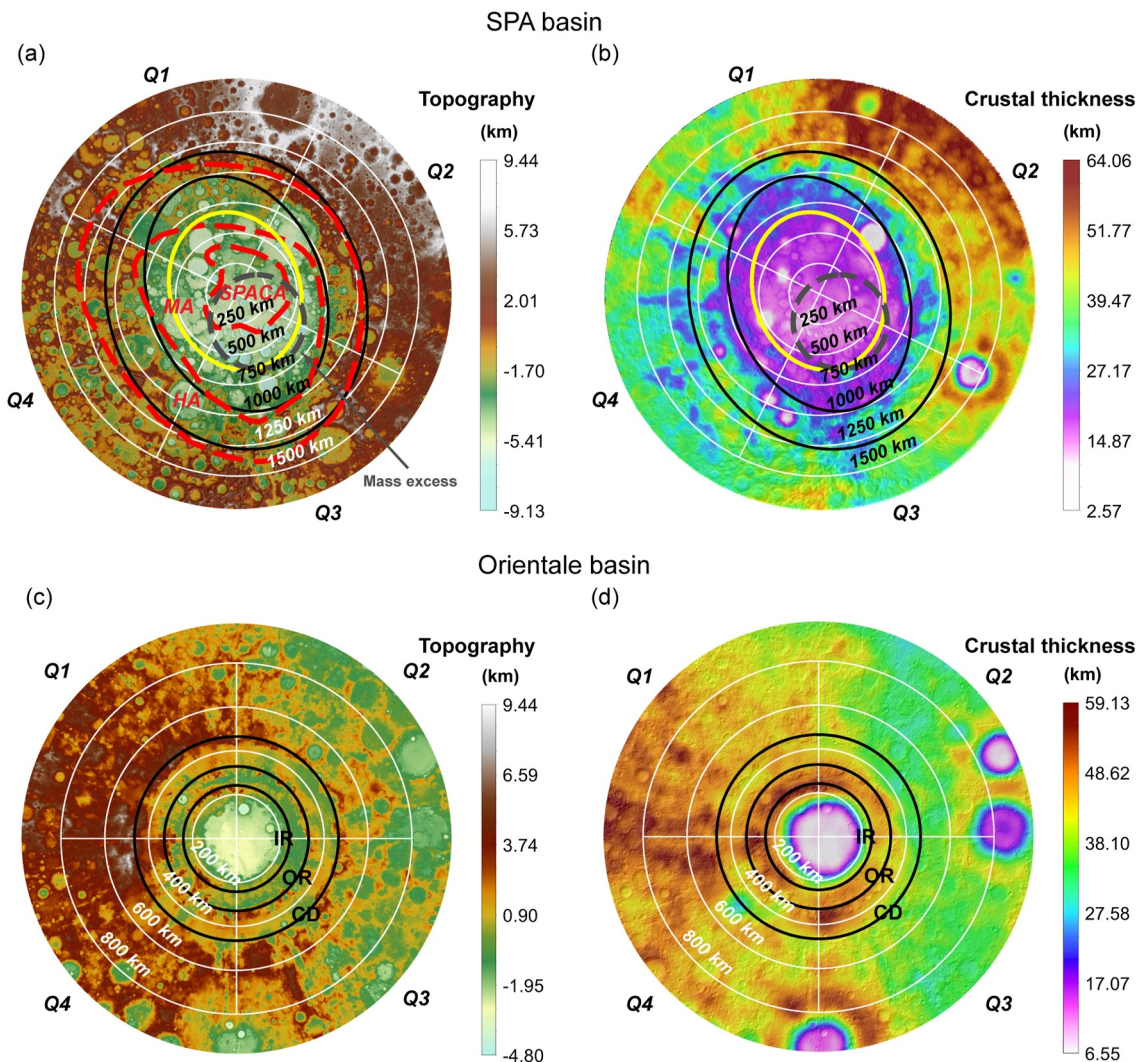


**Figure 3.** Comparison between the South Pole-Aitken (SPA) basin and the Orientale basin in topography, crustal thickness and ring structures. (a, b) are for the SPA basin and (c, d) are for the Orientale basin. The red dashed lines in panel (a) are the boundaries of compositional zones within the SPA basin suggested by Moriarty and Pieters (2018). The solid black lines are the best-fit topographic ellipses (Garrick-Bethell & Zuber, 2009). The solid yellow ellipse in panels (a, b) suggests the possible location of the SPA peak ring estimated by the ring spacing relationship. The dashed gray circle in panels (a, b) marks the mantle mass excess identified by James et al. (2019). The solid black circles in panels (c, d) are the ring structures of the Orientale basin (IR = Inner Rook Ring; OR = Outer Rook Ring; CD = Cordillera Ring). The white lines in all figures divide the area into four quadrants for average topographic measurements (shown in Figure S3 in Supporting Information S1), and the annular sectors show the distance from both basin centers.

impact melt origin for SPACA from the perspective of the scale of the SPA impact melt sheet. Given that most impact melt generated during basin-forming events should be retained within the basin peak ring (e.g., Head, 2010; Petro, 2011), a key to addressing this question is to estimate the possible location of the peak (inner) ring of the SPA basin. The immense size of the SPA basin suggests that it should be a multi-ring basin (e.g., Baker et al., 2012), but its ring structures have been strongly modified and erased. Nevertheless, the large-scale topography of the SPA basin (Figure 3a and Figure S3a in Supporting Information S1) may still provide significant clues. In Figure 3a and Figure S3a in Supporting Information S1, a distinct topographic depression with a relatively flat interior relief can be observed in the center of the SPA basin, and the entire central depression corresponds to the region of relatively thin crust (Figure 3b). James et al. (2019) also noted the existence of a large excess of mass beneath the SPA central depression (gray dashed circle in Figures 3a and 3b). Based on the topography, as well as the distribution of Th and iron (FeO), Garrick-Bethell and Zuber (2009) proposed two best-fit topographic ellipses for the SPA basin structure, which are depicted by black ellipses in Figures 3a and 3b. The region between these two ellipses was also defined as the SPA basin Outer Terrace.



The Orientale basin is the most well-preserved and well-studied multi-ring basin on the Moon (e.g., Head, 1974; Johnson et al., 2016; Spudis et al., 1984). The ring system of the Orientale basin may provide instructive guidance for assessing the ring positions of the SPA basin. The Orientale basin features three concentric rings, from the center of the basin outwards are the Inner Rook Ring (IR), the Outer Rook Ring (OR) and the Cordillera Ring (CD) (black solid circles in Figures 3c and 3d). The geological unit between the OR and the CD is the Montes Rook Formation (e.g., Head, 1974), which is interpreted as a mega-terrace formed by collapse of the basin rim crest area in the latter stage of the basin forming event (e.g., Head, 2010). A central topographic depression (Figure 3c and Figure S3b in Supporting Information S1), characterized by thin crust (Figure 3d; Wiczorek et al., 2013), also occurs in the center of the Orientale basin, lying within the Inner Rook ring.

Assuming that the SPA basin has a broadly similar multi-ring structure to the Orientale basin, the two SPA topographic ellipses are probably equivalent to the IR and OR of the Orientale basin, and the SPA basin Outer Terrace, the region between these two ellipses, is analogous in position to the Montes Rook Formation in Orientale. In terms of composition, the SPA basin Outer Terrace is a compositional transition zone broadly aligned with the Heterogeneous Annulus defined by Moriarty and Pieters (2018) (Figure 3a), exhibiting feldspathic materials mixed with localized pyroxene-bearing materials. This is also consistent with the potential mega-terrace origin for the SPA basin Outer Terrace. Pike and Spudis (1987) pointed out that large basins with concentric rings on the Moon and other terrestrial bodies often show ring spacing approximately proportional to the  $\sqrt{2}$ , with the Orientale basin being the one of the classic examples. Therefore, if the two identified SPA topographic ellipses are treated as the outermost two rings of the SPA basin, following the above ring spacing relationship, we can approximate the location of the SPA peak ring (the yellow ellipse in Figures 3a and 3b; with semimajor axis of 686 km and semiminor axis of 510 km). Indeed, this approximate SPA peak ring is largely coincident with the edge of the central depression as observed in the topography, particularly in the Q3 area (Figure S3a in Supporting Information S1), and the area it encloses is significantly larger than the SPACA region.

Within the Orientale Inner Rook ring (the peak ring of the Orientale basin), the Orientale impact melt sheet is widely exposed, while the mare basalt deposits are mostly concentrated in the centermost region of the basin. There may be a similar material distribution within the possible SPA peak ring. First, the scale of our approximate SPA peak ring is compatible with previous estimates of the volume of the SPA impact melt sheet, which could be on the order of  $10^7$ – $10^8$  km<sup>3</sup> (Potter et al., 2012) with the assumed thickness up to 50 km (Vaughan & Head, 2014), equivalent to a areal extent of at least  $\sim 10^6$  km<sup>2</sup> (a circle with a radius of  $\sim 600$  km) if the geometry of the melt sea is considered as a cylinder. This implies that no additional ring exists inside this approximate peak ring and its interior can be well-filled with the SPA impact melt. Second, we may see the possible presence of the SPA impact sheet within the approximate SPA peak ring but outside the SPACA. On the northern exterior of the SPACA, the original geologic units are strongly obscured by the numerous large impact craters, but on the southern exterior of the SPACA (indicated by white arrows in Figure 4), we note a good candidate region for the exposed SPA impact melt sheet. This region is still within the SPA central depression, but in comparison to the SPACA, it displays a higher albedo (Figure 2i), a higher density of craters (Figure 2j) and a rougher surface (Figure 7a). This region also exhibits clear differences from the SPACA in having predominantly low-Ca pyroxene materials with relatively high Th abundance (Figure 4a), and low FeO abundance (Figure 4b). Furthermore, the elevated Th abundance is essentially confined to this region (Figure 4a). All these features are consistent with the upper layer of a differentiated SPA impact melt sheet inferred by Vaughan and Head (2014).

Overall, we suggest that the scale of the SPACA is too small to be a potential SPA impact melt sheet. In the center of the SPA basin, we may see a similar material distribution similar to that observed in the center of the Orientale basin. The HCP-bearing SPACA may only represent the centermost deposits of mare (including cryptomare) basalt in the SPA basin center overlying the SPA impact melt sheet, and the area surrounding it is probably the exposed SPA impact melt sheet that is characterized by LCP-rich and high Th abundance in composition.

### 3.2. Assessing Evidence for More Extensive Cryptomaria in the SPACA

Here, we assess the alternative hypothesis for the volcanic origin of the SPACA. Although previous studies have already identified several patchy maria (Pasckert et al., 2018) and cryptomaria (Whitten & Head, 2015a) in the center of the SPA basin, it is apparent that the mafic (HCP) anomaly represented by the SPACA is much more widespread. Within our current understanding, HCP-rich materials exposed on the Moon could be in association with (a) mare or cryptomare basalt deposits, (b) differentiated impact melt sheet or c) potential lunar crust

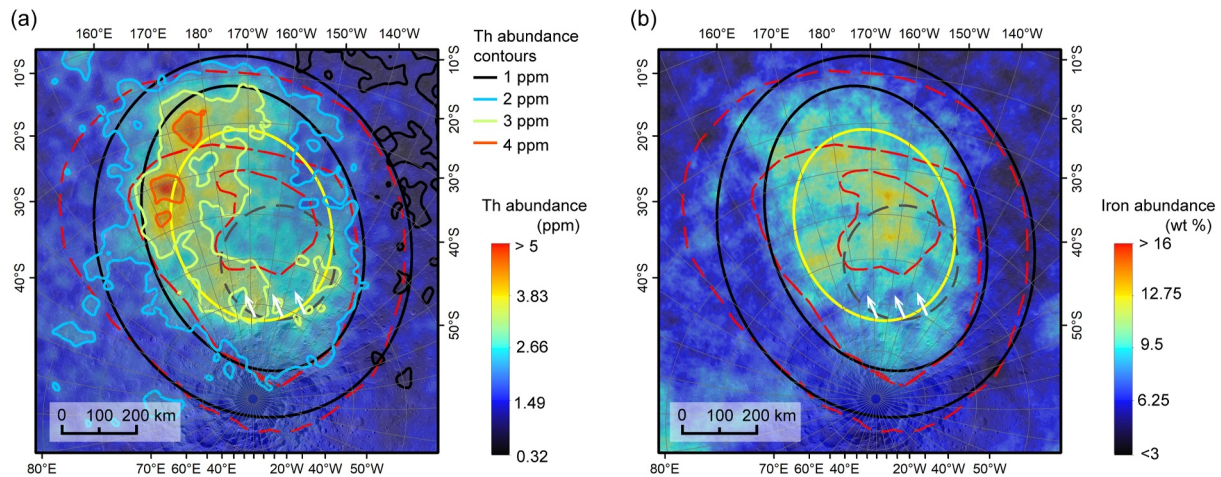


**Figure 4.** The distribution of Th and iron in the region south of the SPACA and the entire basin. (a, b) are the Th and iron distributions detected by the LP GRS. The red dashed lines indicate the boundaries of compositional zones within the South Pole-Aitken (SPA) basin (Moriarty & Pieters, 2018). The solid black lines are the best-fit topographic ellipses (Garrick-Bethell & Zuber, 2009). The solid yellow line suggests the possible location of the SPA peak ring, which is described in Section 3.1 and Figure 3. The dashed gray circle indicates the mantle mass excess (James et al., 2019). Note that in the region south of SPACA (indicated by white arrows), the abundance of Th and iron varies significantly between the two sides of the boundary. This region is characterized by an increase in Th abundance and a decrease in iron abundance. In addition, the elevated Th abundance in this region is essentially confined within the possible peak ring. We show that the region south of SPACA likely represents the deposits of SPA impact melt.

component (Ogawa et al., 2011; Yamamoto et al., 2015). Crust-origin HCP materials are often mixed with feldspathic materials and mostly occurs in the lunar highlands (Ogawa et al., 2011; Yamamoto et al., 2015), whereas SPACA is located in the center of a giant basin and the HCP distribution is relatively continuous and widespread. Our analysis above also suggests that the SPACA may not be the differentiated SPA impact melt sheet unit due to its small areal extent relative to the expected SPA impact melt sheet. Under this scenario, the SPACA likely represents a more extensive range of volcanic deposits in the SPA basin center. Several supporting evidence for the more widespread volcanic resurfacing events occurring in the SPA basin center are found.

Apollo peak-ring is the largest ring structure within the SPA basin, located on the northeast of the SPACA, while no distinct ejecta blanket of the Apollo basin appears to be observed in the SPA basin center or the SPACA region in the large-scale surface topography (Figure 2b) and morphology (Figure 5a), where instead we can observe relative flat (Figure 2b) and low-slope terrain (Figure 2d). Nevertheless, the topography of the SPACA (Figure 2b) still shows an obvious north-south variation: the northern portion of SPACA is generally ~1 km higher than the southern portion. This may be attributed to the effect of the younger superposed Apollo impact basin (Ivanov et al., 2018) and its ejecta deposits. We used the ejecta decay models (McGetchin et al., 1973; Pike, 1974; Sharpton, 2014) to test this hypothesis (see Text S1 in Supporting Information S1). As shown in Figure 5b and if Pike's Model and Sharpton's model can provide better estimates of ejecta thickness than McGetchin's Model (e.g., Fassett et al., 2011; Xie & Zhu, 2016; Xu et al., 2021; also see details in Text S1 in Supporting Information S1), it suggests that the Apollo basin ejecta deposits did contribute to shaping the SPACA topography and was able to create a 0.5–1 km difference in north-south elevation as we can observe. In this case, the probable reasons for the missing morphology of the Apollo basin ejecta blanket within the SPACA region could be strong degradation or resurfaced by subsequent events. In fact, the impact ejecta morphology of the Apollo basin may be observable beyond the northeastern rim of the basin (Figure 5a), while it is almost invisible on the southwestern side of the basin. Thus, we may exclude the factor of the degradation of the Apollo basin ejecta blanket. As for being resurfaced, a specific example can be seen in the adjacent region to the south of the Apollo basin rim (Figure 5a), which has already been identified as cryptomare deposits by Whitten and Head (2015a, 2015b). This region appears as very flat terrain much more similar in smoothness to the mare region on the Apollo basin floor just north of the southern Apollo rim (Figure S4 in Supporting Information S1), rather than the rugged terrain commonly formed by impact ejecta. Some other flat, low-slope regions within the SPACA region may have a similar origin.

Widespread resurfacing events occurring within the SPACA region can also be revealed by the crater size-frequency distribution (CSFD) analysis. We performed CSFD measurements on craters >5 km in diameter

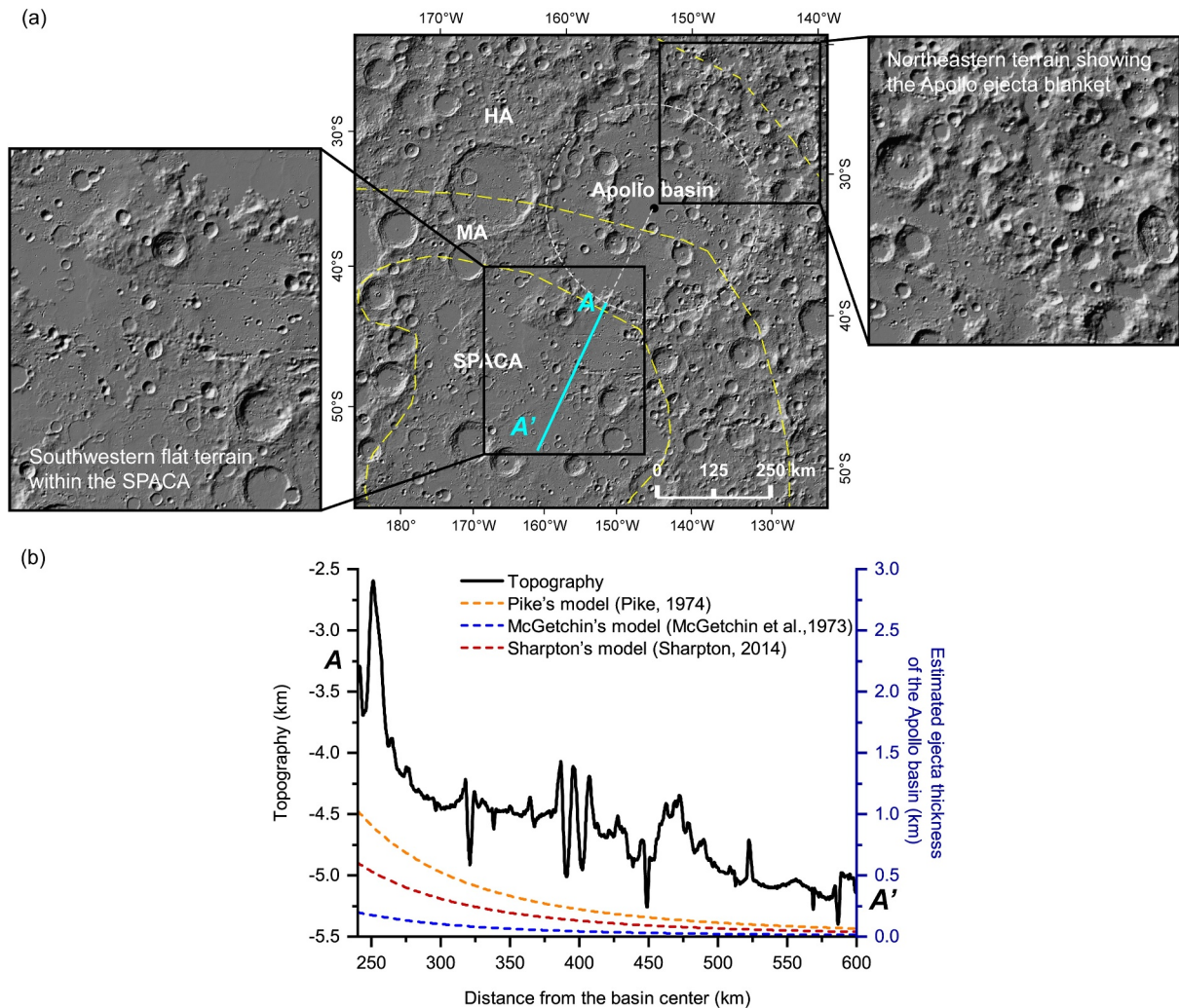


**Figure 5.** Ejecta deposits of the Apollo basin. (a) is shaded relief map derived from SLDEM2015 data. AA' marked in panel (a) is a radial topographic profile line. The yellow dashed lines in panel (a) indicate the compositional zones. The zoom-in panels display the topographic details of the terrain northeast (the possible Apollo ejecta blanket) and southwest (flat terrain within the SPACA) of the Apollo basin. (b) shows the comparisons of the real AA' topographic profile and the estimated Apollo ejecta thickness calculated by three models (McGetchin et al., 1973; Pike, 1974; Sharpton, 2014).

(Head et al., 2010; Povilaitis et al., 2018) in the three SPA interior compositional zones (Figure 6). Although the compositional zones, by definition, represent only the upper microns of the lunar surface, the differences in composition also reflect differences in origin. CSFD analysis of them can show variations in evolutionary paths and age differences among them. The cumulative CSFD plots for the three compositional zones within the SPA basin are shown in Figure 6b. We performed the Kolmogorov-Smirnov (K-S) test (e.g., Noether, 1978) on the CSFD plots for the MA and HA to determine whether the distributions of the two sample groups are the same. Results of the K-S test between the MA and HA plots provide a p-value of 0.9985, indicating that the CSFD shapes for the MA and HA are statistically indistinguishable as well as the spatial density of craters ( $9.6 \pm 0.2 \times 10^{-4} \text{ km}^{-2}$  and  $9.2 \pm 0.3 \times 10^{-4}$ , respectively). This is consistent with their interpretation as SPA impact melt and SPA basin deposits. The relative paucity of large craters within the SPACA is apparent in Figure 6a. While the CSFD shape for large (>20 km) craters within the SPACA is statistically indistinguishable (K-S test p-value of 0.8685) from the annulus units (both individually and combined), the spatial density of such large craters in the SPACA ( $1.2 \pm 0.2 \times 10^{-4} \text{ km}^{-2}$ ) is less than in the annulus units combined ( $1.7 \pm 0.1 \times 10^{-4} \text{ km}^{-2}$ ). Despite the modest number of large craters in the SPACA, this difference is statistically significant at the two-sigma level. The observed younger crater retention age of the SPACA suggests that this region was resurfaced. For smaller craters, down to 5 km, the CSFD in the SPACA is steeper than for the annuli



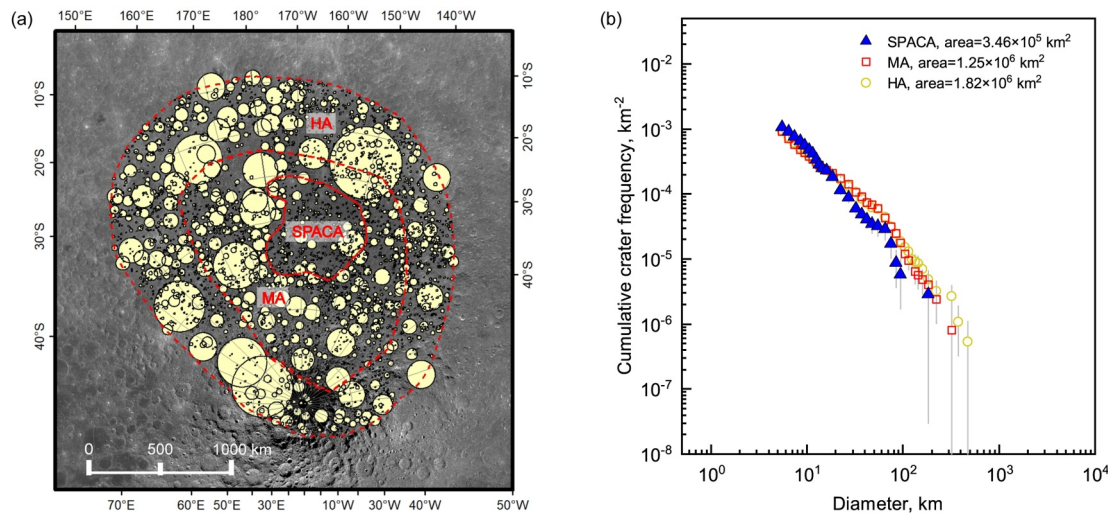


**Figure 6.** Distributions of craters  $\geq 5$  km in diameter within the South Pole-Aitken (SPA) basin and the corresponding crater size-frequency distribution (CSFD) analysis. The craters shown in panel (a) are from Povilaitis et al. (2018) (5–20 km in diameter) and Head et al. (2010) ( $>20$  km in diameter), and (b) shows the cumulative CSFD plots for the three compositional zones within the SPA basin. Note that the distribution patterns for the Mg-pyroxene Anulus and Heterogeneous Anulus are comparable, while the plot for the SPACA shows a clear deflection at  $\sim 70$  km diameter, strongly suggesting that resurfacing events occurred at the SPACA.

(Figure 6b), and the K-S test indicates that this difference is statistically significant. In contrast to the large craters, the spatial density of craters  $>5$  km in the SPACA ( $10.7 \pm 0.6 \times 10^{-4} \text{ km}^{-2}$ ) is greater than in the annuli; this difference is statistically significant at  $\sim 1.5$  sigma level. Preferential obliteration of old smaller craters can be responsible for shallower CSFD for the older annulus, but it cannot explain the higher crater density on a younger SPACA. A possible explanation is that the old relatively small degraded craters are easier to identify on the topographically smoother and more coherent SPACA terrain (Wu et al., 2022).

The above observation on surface morphology and the CSFD analysis demonstrate a history that the SPA basin center was widely resurfaced. Yet more than one resurfacing event may have occurred to such a large extent of the SPACA (e.g., Head & Wilson, 2017), which is also supported by the geological maps compiled by Ivanov et al. (2018) and Poehler et al. (2020), at least including the age of Early Imbrian and Late Imbrian. In the later section, we provide a more detailed estimate of the age in different subregions (Section 4.2). As aforementioned, the HCP anomaly of the SPACA should have a volcanic origin, namely in association with mare or cryptomare deposits. Given the fact that most of the SPACA region (excluding the identified mare patches) displays a higher albedo compared to typical maria but lower than lunar highlands, as well as the generally older ages on the geological maps (Ivanov et al., 2018; Poehler et al., 2020), the more extensive resurfacing events occurring in the center of the SPA basin likely suggest the presence of more unrecognized cryptomare deposits.

Distal and proximal ejecta from multiple sources may have contributed to the brightened surfaces of these ancient basalts, eventually forming the extensive SPA central cryptomaria. Within the SPACA region, several clear secondary crater clusters and chains (Figure 7a) can be traced back to the Orientale basin (also see Figure 6 in Guo et al., 2018), indicating that distal ejecta from the Orientale basin could affect a significant portion of the SPACA terrain, particularly to the eastern side, and is the important source of the higher-albedo deposits on the SPACA surface. Meyer et al. (2020) also pointed out that the Orientale basin ejecta could spread more laterally to form larger light plains due to the potential preexisting smooth surfaces (likely related to the cryptomare deposits suggested in this work), similar to the case with the cryptomaria to the southeast of the Orientale basin. In the western side of the SPACA terrain, as indicated in the OMAT map (Figure 2g), a series of relatively young impact craters, such as Finsen (Late Imbrian), Alder (Early Imbrian) and Abbe H (Eratosthenian), could have emplaced a large quantity of proximal ejecta on the SPACA surface, resulting in the much brighter western SPACA terrain. In addition, an obvious north-south ejecta ray from an unknown source (perhaps the Jackson crater) is also observed on the OMAT map, crossing over the middle part of the SPACA terrain, including the Bhabha/Mons Marguerite area.

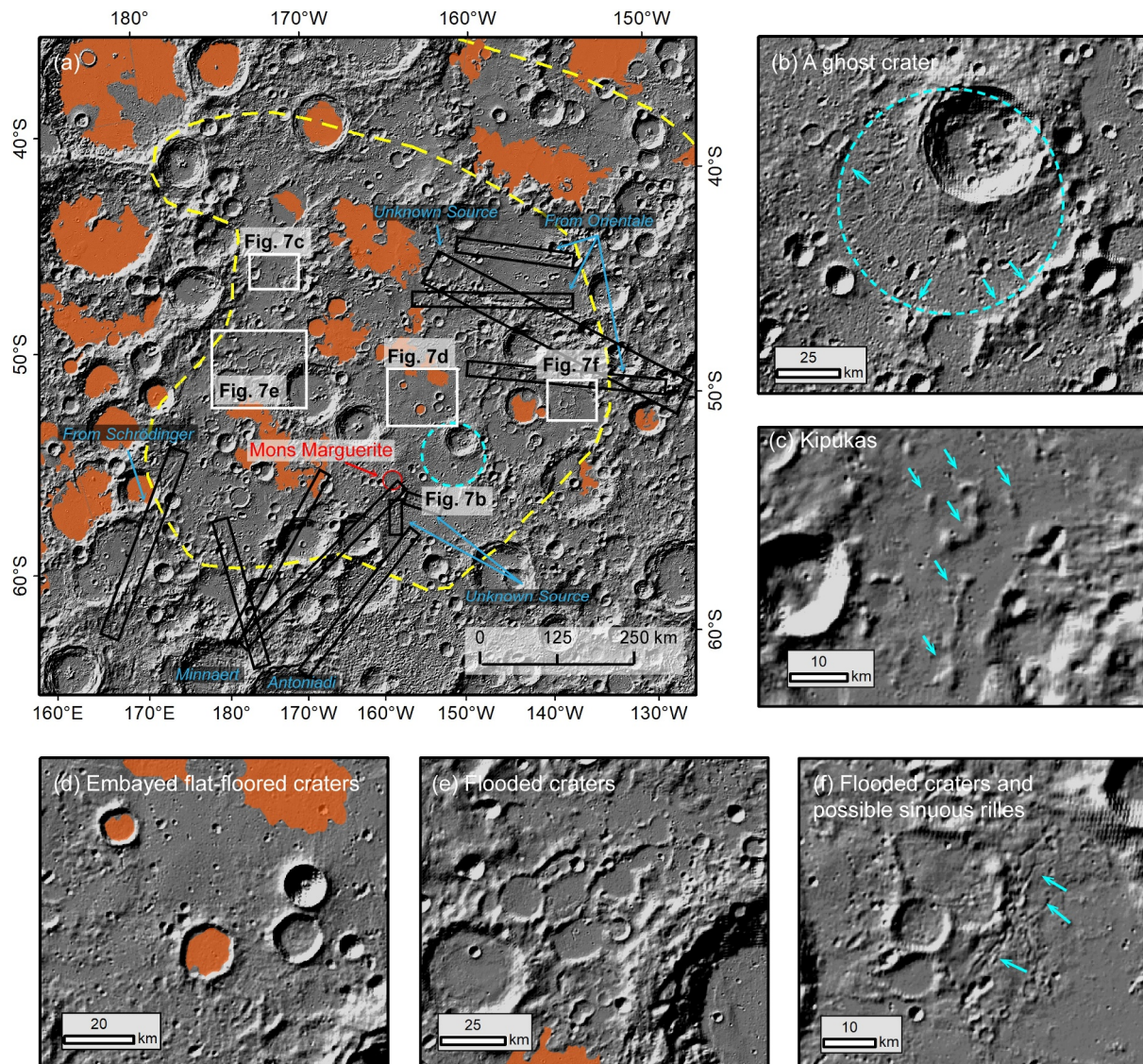


**Figure 7.** Additional geomorphological observations for resurfacing events occurring at the center of the South Pole-Aitken (SPA) basin. (a) Shaded relief map derived from SLDEM2015 data. The areas in orange are the previously identified younger maria (Nelson et al., 2014). The yellow dashed lines are the boundaries of the SPA compositional zones (Moriarty & Pieters, 2018). Examples of secondary crater clusters and chains from the Orientale basin (Guo et al., 2018) and other source craters are marked with black boxes. It can also be seen that the surface of the region located south of the SPACA is clearly rougher than that of the SPACA and has a high density of small craters, suggesting that resurfacing events may not have occurred here. (b) An unnamed ghost crater (impact crater formed in the SPACA and subsequently flooded to near the rim crest by additional cryptomaria) about 98.72 km in diameter. Cyan arrows indicate the possible rim remnants of this ghost crater. (c) Examples of embayed kipukas (plains-flooded topographic prominences) marked with cyan arrows. (d) Examples of embayed flat-floored craters with younger basalt infilling. (e) Flooded craters west of the SPACA. (f) Several flooded craters on the floor of a large basin with possible sinuous rilles appearing nearby.

## 4. Additional Characterization and Synthesis of the Nature of SPACA and the Interpreted SPA Central Cryptomaria

### 4.1. Identification of the SPA Central Cryptomaria

The ancient SPA basin has a complex history of formation, geological evolution and modification (e.g., Garrick-Bethell & Zuber, 2009; Moriarty & Pieters, 2018; Potter et al., 2012), and due to its ancient age (Hiesinger et al., 2012), post-basin impact excavation and lateral ejecta distribution may have blurred the exact boundaries of any cryptomare deposits that may be present. In some cases, thick ejecta deposits may even have made some cryptomare deposits invisible due to burial. Nevertheless, subsequent impact excavation could provide essential



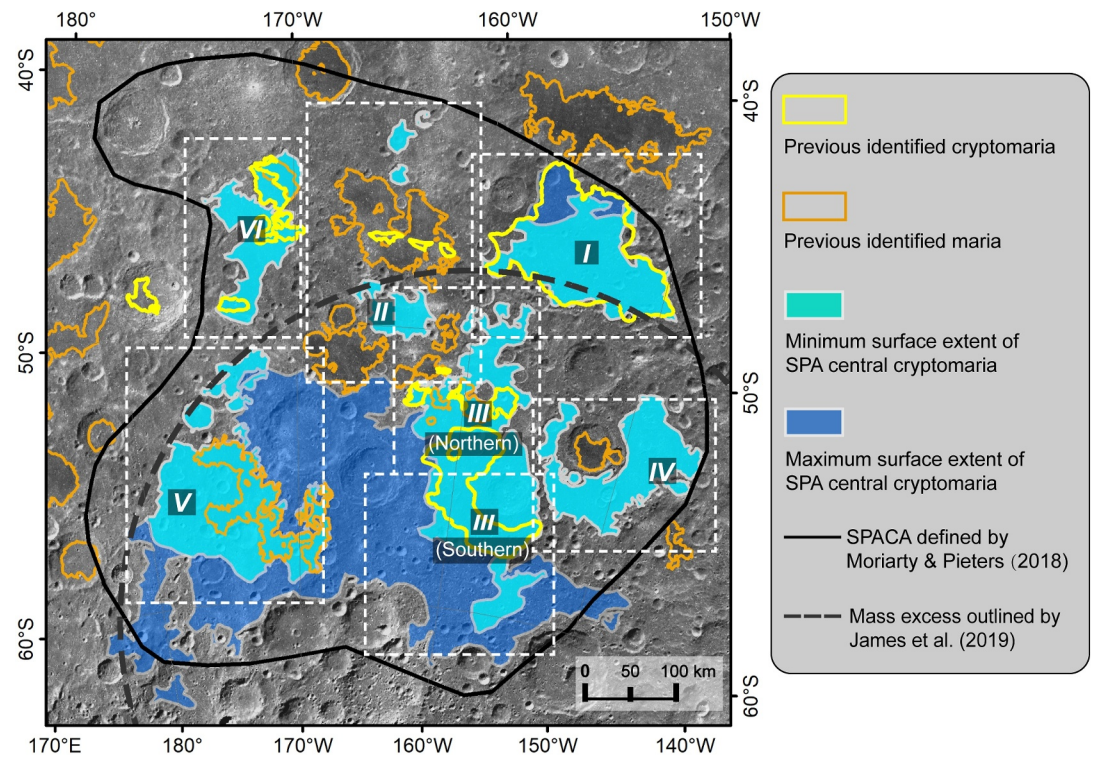


**Figure 8.** Areal extents of the South Pole-Aitken (SPA) central cryptomaria. The areas marked in orange are the previously identified younger mare deposits (Nelson et al., 2014), and the areas outlined by yellow solid lines are the previously identified cryptomare deposits (Whitten & Head, 2015a). The areas shown in cyan and blue are the areal extents of the SPA central cryptomaria identified in this work. Areas in cyan indicate the minimum surface extents, which correspond to the characteristics of HCP composition, low slope ( $<5^\circ$ ), intermedium albedo and intermedium surface roughness. Areas in blue suggest the possible maximum surface extents, mapped on the basis of the distribution of areas of HCP composition; they include large impact craters likely postdating the cryptomare emplacement. White dashed boxes and numbers correspond to each area shown in Figure S5 in Supporting Information S1.

clues to the existence of cryptomaria at depth, as their ejecta and crater walls would expose the composition of the cryptomaria (e.g., Whitten & Head, 2015a, 2015b). Based on a synthesis of topography, composition, albedo and surface roughness, we mapped the possible minimum and maximum extent of the SPA central cryptomaria (Figure 8).

As described in Section 3.1, the initial substrate in the central SPA basin could be predominantly LCP-bearing impact melt. Any HCP-bearing materials observed within the SPACA could thus be linked to later volcanic plains or the excavation of these volcanic materials by later impacts. The exposure of HCP-bearing materials associated with ejecta and walls of these subsequent craters should be an excellent indicator of cryptomare or mare presence, distribution and geometry. On the pyroxene composition map obtained from Kaguya MI data (Figure 2e), we outlined all the regions within the SPACA showing spectral features of HCP. We interpret these regions as likely representing the maximum extent of the SPA central cryptomaria. They include large impact craters likely postdating the cryptomare emplacement and possibly superposed over the cryptomare materials.

Within this maximum range, we further delineate the minimum extent of the SPA central cryptomaria. If the cryptomare deposits are less affected by large impact craters, their surface topography could be relatively flat on the slope map (such as a slope  $<5^\circ$  in Figure 2d; Kreslavsky et al., 2013). On the other hand, their surface could also display intermediate albedo (Figure 2h; higher than typical maria but lower than lunar highlands) and intermediate surface roughness (Figure 2i; also higher than typical maria but lower than lunar highlands). The cyan areas in Figure 8 are the areas within the SPACA that meet all the above characteristics and are considered to represent the most likely minimum extent of the SPA central cryptomaria.



#### 4.2. Regional Investigations of Age, Thickness and Volume

It is unlikely that the SPA central cryptomaria candidates that we have identified over such a large extent (Figure 8) represent only a single eruptive phase (e.g., Head & Wilson, 2017). To determine the local age, thickness and volume, we divided the identified cryptomaria into six regions (Figure 8) based mainly on the distribution locations and some apparent deposit differences, such as crater density (Figure 2j), and then conducted a detailed analysis of each region. The new geological maps of the SPA basin (Ivanov et al., 2018; Poehler et al., 2020) were also employed here to obtain the relative ages of the cryptomaria. The main method utilized to determine the cryptomare thickness is based on excavation depths of the largest impact craters in each subregion that excavated basaltic (HCP) material. In most regional investigations in this work, we were unable to observe a penetrating crater that excavated into the possibly LCP-bearing underlying layer. Therefore, the thickness calculated using this method only indicates the minimum estimate. The excavation depth  $H_e$  of a crater with a transient diameter of  $D_t$  can be obtained by the equation (Melosh, 1989):

$$H_e = \frac{1}{10} D_t.$$

The relationship between the transient diameter  $D_t$  and the rim-crest diameter  $D$  can be further calculated by

$$D_t = \begin{cases} 0.84D, & \text{if } D < 15 \text{ km (Melosh, 1989)} \\ D_Q^{0.15} D^{0.85}, & \text{if } D > 15 \text{ km (Croft, 1985)} \end{cases},$$

where  $D_Q$  is the simple-complex transition diameter, which Croft (1985) suggested as 15 km for lunar craters. In one case, we also estimated the thickness using the PBC method in Yingst and Head (1997) (see Figure 4 in the literature), which is a geometric calculation according to the diameters of rim crest, interior basalt filling and crater floor, and the relevant crater parameters were given by Pike (1974, 1977).

**Region I:** This region is located south of the Apollo southern rim (Figure S5a in Supporting Information S1), and was identified as cryptomare deposits by several previous studies (e.g., Pieters et al., 2001; Whitten & Head, 2015a, 2015b). As aforementioned, Region I is a flat terrain similar in topography to the mare to north of the rim, rather than a rugged ejecta blanket terrain (see also Pieters et al., 2001; their Figure 12b and Figure 13) (Figure S4 in Supporting Information S1). This constrains the resurfacing event occurring here to post-Apollo basin formation, namely after  $3.98^{+0.04}_{-0.06}$  Ga in pre-Nectarian (from Ivanov et al. (2018) using the production function and chronology function from Neukum et al. (2001)), with the Apollo ejecta blanket is buried underneath. In addition, the surface of Region I has been modified by Orientale secondaries (Guo et al., 2018; Pieters et al., 2001; Figure 7a), indicating that the cryptomare here was emplaced before formation of Orientale basin ( $3.80^{+0.0074}_{-0.0079}$ , newly dated by Yue et al. (2020) based on the production function and chronology function from Neukum (1983), representing the end of Early Imbrian). The spectral analysis shows that parts of the eastern wall and ejecta of the White crater also have HCP-bearing features (Figures S5b and S6a in Supporting Information S1), which we interpret as the result of local cryptomare excavation. Such a scenario would further constrain the age of the local cryptomare to be prior to the formation of White crater, classified as Nectarian on the recent geological maps (Ivanov et al., 2018; Poehler et al., 2020). More cryptomare could exist in the area adjacent to the Apollo basin southern rim (the white box in Figures S5a and S5b in Supporting Information S1). Although this part is dominated by LCP surface materials, it is still characterized by a very low regional slope. Several craters within this area excavate HCP materials that we interpret to be indicative of additional cryptomare (see also Pieters et al., 2001). When this area is included, the extent of cryptomare we identified in Region I is almost identical to that identified by Whitten and Head (2015a) (Figure 8).

The largest crater in Region I (Figure S5a in Supporting Information S1) did not penetrate into the underlying layer. Therefore, the excavation depth ( $\sim 1.00$  km) of the largest crater (11.86 km in diameter) within Region I is treated as the minimum thickness of the cryptomare.

**Region II:** This region is surrounded by several younger maria. Compared with these maria, Region II has a rougher surface strongly modified by numerous crater chains. The characteristics of relatively low albedo and HCP composition together imply the presence of a cryptomare deposit (Figures S5c and S5d in Supporting

Information S1). Due to the fact that penetrating impact craters are not observed, the excavation depth ( $\sim 0.33$  km) of the largest non-penetrating crater ( $\sim 3.98$  km in diameter) is considered a minimum thickness estimate for the local cryptomare.

We also investigated whether cryptomare exists beneath the surrounding young mare areas. However, confident observations were only found within the large mare area to the north of Region II. The walls of a flat-floored crater show clear LCP spectral features, suggesting that there may be no additional cryptomare deposits buried deeper. We note that Whitten and Head (2015a) identified several cryptomare deposits within this young mare area (Figure 8), which is along a secondary crater chain with relatively high albedo. However, we suggest that these regions may simply be the young mare surface modified by bright ejecta secondaries, showing a surface morphology similar to cryptomaria.

In addition, there are several patches of cryptomare we identified in more northern areas (the white box in Figures S5c and S5d in Supporting Information S1). However, the small size of these deposits does not allow an accurate thickness estimation. Nevertheless, given that these patches are located within a large area of low-slope terrain, a more extensive cryptomare might exist covered by thick ejecta deposits.

*Region III:* Region III occupies a large area on the east side of SPACA, and we divided it into northern (Figures S5e, S5f, S6c in Supporting Information S1) and southern (Figures S5g, S5h, S6d in Supporting Information S1) portions for separate investigation. Whitten and Head (2015a) identified several small cryptomare deposits in the northern portion of Region III (Figure 8), while we note more low-slope terrain in this region (Figure 2d). On the walls of two large fresh craters that are within this northern portion but outside the young mare areas, the presence of HCP-bearing spectral features indicates the cryptomare deposits likely exist in this region (HCP1 and HCP2 in Figures S5e, S5f and S6c in Supporting Information S1), and the mixing with LCP-bearing materials suggests that these two fresh craters may have penetrated through the local cryptomaria into the underlying LCP-bearing layer. We can also observe HCP-bearing spectral features on the walls of several flat-floored craters in the northern portion of Region III (Figures S5e and S5f in Supporting Information S1), which implies that these craters may have impacted into local older cryptomare deposits, and their interiors were then filled with younger mare basalts. Thus, these craters are also treated as impact craters that excavated the cryptomare, and the excavation depth of the largest crater,  $\sim 15.27$  km in diameter, is used to estimate the minimum thickness of the local cryptomare deposits of  $\sim 1.52$  km which is much thicker than the 100 m younger mare deposits reported by Pasckert et al. (2018). Considering that these flat-floored craters are Early Imbrian and the younger interior maria are Late Imbrian on the geological map (Ivanov et al., 2018; Poehler et al., 2020), the age of local cryptomare should be Early Imbrian or earlier.

A ghost crater with a diameter of  $\sim 98.72$  km occupies most of the southern portion of Region III (Figure 7b and Figures S5g and S5h in Supporting Information S1). The entire area shows HCP-bearing features with apparent low albedo, suggesting that the ghost crater could have provided significant space for the potential infilling of the cryptomare. Another large crater, Stoney, with a diameter of 47.4 km is nested inside the ghost crater. Spectral analysis suggests that the band centers of the materials exposed within the Stoney crater (except for the central peak) shift to the longer wavelengths rather than LCP (Figure 6d), probably resulting from the excavation of the preexisting cryptomare deposits in the ghost crater. If Stoney has a Nectarian age as suggested by the geological map (Ivanov et al., 2018; Poehler et al., 2020), the cryptomare in the southern portion of Region III should have occurred in Nectarian or earlier. Its old age is also supported by the fact that the surface of the southern portion of Region III has a generally higher crater density than that of the northern portion (Figure 2j), which has been resurfaced by younger maria in several patches. Since this large ghost crater is almost completely buried, the thickness of the cryptomare outside the ghost crater should approach the original rim height of the ghost crater. According to the relationship between rim height and rim-crest diameter proposed by Pike (1977), the ghost crater has a rim height of  $\sim 1.47$  km. Such a thickness is also supported by the nearby largest non-penetrating crater (11.70 km in diameter), which was excavated to a depth of  $\sim 0.98$  km. Furthermore, the cryptomare filling in the ghost crater's interior might be deeper, yet would not exceed its maximum original crater depth, which is  $\sim 4.14$  km according to Pike (1974). This is also in accordance with the Stoney crater excavation depth of  $\sim 3.96$  km. However, this thickness could be significantly overestimated due to heavy degradation and possible filling with other ejecta. In addition, we favor to interpret the HCP features of the wall and ejecta of the Bhabha crater as being due to the excavation to depths of the thick cryptomare deposits near the southern portion of

Region III, and its LCP-bearing central peak could represent the LCP-bearing SPA impact melt layer buried deep beneath the cryptomare deposits in the center of the SPA basin.

Compared to the previously identified cryptomaria in Region III by Whitten and Head (2015a), we provide a much larger ( $\sim 3$  times) surface extent of the potential cryptomare deposits in the region (Figure 1). Indeed, they also outlined the large cryptomare deposit in the southern portion where we suggest the presence of a ghost crater.

**Region IV:** Region IV is a large impact basin  $\sim 190$  km in diameter overlaid by the Baldet crater. Pasckert et al. (2018) identified two patches of mare regions on the basin floor (their units *Ba3* and *Ba4*; marked by white boxes in Figures S5i and S5j in Supporting Information S1). However, the authors point out that *Ba4* is significantly brighter than other mare units in the area, with a lower FeO content, while the age and thickness of *Ba4* were not calculated. This implies that the *Ba4* unit may represent parts of the cryptomare deposits on the basin floor. We infer that the cryptomare is more widely distributed on the basin floor, as the overall topography of the basin interior is flat with a  $1\text{--}2^\circ$  slope and the basin interior is also HCP in composition with similar low albedo (average of 0.092 at  $M^3$  1,498 nm band nm) to other typical cryptomares. Several flooded craters and the craters excavating HCP-bearing materials can be observed outside *Ba3* and *Ba4* areas, further supporting the more extensive cryptomare filling in the basin. We take the excavation depth of the largest DHC ( $\sim 19.12$  km in diameter), which is  $\sim 1.84$  km, as the minimum thickness of the cryptomare.

Different from the Stoney crater in Region III, the wall and rim of the Baldet crater show LCP-bearing features (Figure S6e in Supporting Information S1), and its rim appears to be cut and embayed by the subsequent exterior resurfacing units. Therefore, the age of the cryptomare deposits on the basin floor should be younger than that of the Nectarian-aged Baldet crater (Ivanov et al., 2018; Poehler et al., 2020). We have no other observations to further constrain its age, but because of its brighter and rougher surface compared to the Late Imbrian-aged Baldet interior mare, we favor an Early Imbrian age for the cryptomare, which is also the age of *Ba4* on the geologic map.

**Region V:** We further divided Region V into three subregions V-A, V-B and V-C, as shown in Figures S5k and S5l in Supporting Information S1. Most parts of the surface of Region V-A are covered by low-albedo younger mare deposits, while the remaining parts are heavily modified by impact craters, making it difficult to determine the extent of potential local cryptomare. Thus, we only outlined the area with relatively low albedo as the most likely cryptomare extent. In fact, it could be much larger since the HCP features appear to extend more widely over flat terrains but are obscured by the large amounts of ejecta deposits. Moreover, a fresh crater  $\sim 9$  km in diameter (with excavation depth of  $\sim 750$  m) near the younger mare region also shows an HCP feature. This could indicate that this crater penetrated into an underlying cryptomare layer, as the thickness of the young mare is less than a hundred meters (Pasckert et al., 2018). On the basis of these relationships, we interpret the local cryptomare to also extend beneath the young mare region. HCP features can also be seen in several large craters in the middle of Region V-A, lying outside the young mare area. Because most of them are degraded or superimposed, we choose a relatively young crater with diameter of  $\sim 19.00$  km to estimate the thickness of the local cryptomare, which is  $\sim 1.83$  km.

Region V-B is a small area north of Region V-A, with several features (such as flooded craters and kipukas) visible on the surface (Figure 7e). To be conservative, we outlined only the area with relatively low albedo. As this region is adjacent to the Alder crater, the thick proximal ejecta deposits from Alder may completely bury the local cryptomare. We used the largest fresh crater ( $\sim 5.58$  km in diameter) within this region to calculate the minimum thickness of the local cryptomare, which is  $\sim 0.47$  km. It is also possible that Region V-B and Region V-A were a single deposit but were separated by thick ejecta deposits on the surface.

Region V-C is the floor of an isolated crater. The entire crater floor shows HCP features except for a fresh crater  $\sim 4.47$  km in diameter excavating LCP-bearing materials (Figure S6f in Supporting Information S1), suggesting that the thickness of the cryptomare here is less than  $\sim 0.03$  km.

We adopt the ages for the entire Region V on the geological map (Poehler et al., 2020), which is Early Imbrian. This is consistent with the fact that the surface of parts of these regions is ejected by the Early Imbrian-aged Alder crater (e.g., Figure 2g).

**Region VI:** Yingst and Head (1997) identified this region as one of the mare ponds within the SPA basin, and Whitten and Head (2015a) also suggested the presence of several cryptomare deposits in the north (Figure 1). A flat-floored crater in the region has walls showing LCP characteristics in composition (Figures S5m, S5n, S6g in Supporting Information S1). A younger small DHC on the floor indicates that the interior of this flat-floored crater



**Table 1**

*Age, Areal Extent, Thickness, Volume Estimates for South Pole-Aitken Central Cryptomaria and Their Corresponding Roughness and Albedo*

Region	Subregion	Cryptomare age (up to)	Cryptomare area ( $\times 10^4$ km <sup>2</sup> )	Cryptomare thickness (km)	Cryptomare volume ( $\times 10^4$ km <sup>3</sup> )	Surface area identified by Whitten and Head (2015a)	Roughness			Albedo	
							0.115 km	0.46 km	1.84 km	LOLA	M <sup>3</sup> 1,498 nm
I	—	Nectarian	1.44	1.00	1.44	1.76	0.83	1.07	0.92	0.208	0.090
II	—	Early Imbrian	0.30	0.33	0.01	0.04	0.83	0.89	0.78	0.223	0.112
III	Northern portion	Early Imbrian	1.28	1.52	1.95	0.11	0.82	0.84	0.62	0.209	0.089
	Southern portion	Nectarian	1.39	1.47	2.04	0.75	0.81	0.99	0.93	0.211	0.086
IV	—	Early Imbrian	1.17	1.84	2.15	—	0.89	1.03	0.72	0.215	0.092
V	A	Early Imbrian	1.92	1.83	3.51	—	0.87	0.78	0.69	0.223	0.102
	B		0.21	0.47	0.10	—					
	C		0.08	0.38	0.03	—					
VI	—	Early Imbrian	0.91	0.65	0.59	0.23	0.82	0.75	0.49	0.221	0.111

was filled with basalt. The exterior of this flat-floored crater could be embayed by more cryptomare; the floor appears like the rest of the unit as the basaltic spectral features are visible in other areas of the region. Some embayed kipukas can also be seen within this region (Figure 7c). The relatively high local albedo is likely attributed to the proximal ejecta deposits from nearby craters, such as the Eratosthenian-aged Finsen crater and the Early Imbrian-aged Alder crater, implying that the cryptomare age may be Early Imbrian or earlier.

On the basis of the geometry of the flooded flat-floored crater (~20.89 km in diameter), we estimated that the thickness of the cryptomare deposit outside the flat-floored crater could reach ~0.65 km, which is also supported by the excavation depth (~0.52 km) of the largest fresh craters (~6.21 km in diameter) within Region VI excavating HCP-bearing materials.

**Summary:** The results described above are summarized in Table 1. We provide a significant expansion to the cryptomare deposits previously identified in the center of the SPA basin by Whitten and Head (2015a). Our regional analysis suggests that the SPA central cryptomare deposits may cover an areal extent of at least  $8.7 \times 10^4$  km<sup>2</sup>, three times larger than that estimated by Whitten and Head (2015a) ( $2.96 \times 10^4$  km<sup>2</sup> in total). Our results also indicate that the older cryptomare deposits (essentially over 1 km in thickness) are much thicker than the young mare deposits (generally <100 m; Pasckert et al., 2018), in agreement with the earlier overall thickness estimate of ~1.5 km (Whitten & Head, 2015a) and the prediction of 1–2 km cryptomare deposit thickness by the flooding model (Whitten & Head, 2013). Applying the cryptomare thicknesses to the surface areas of each region shown in Table 1, a minimum total volume of  $\sim 1 \times 10^5$  km<sup>3</sup> for the entire SPA central cryptomare deposits can be estimated. Based on the stratigraphic relationship of relevant units on the most recent geological maps (Ivanov et al., 2018; Poehler et al., 2020), we also estimate the ages for these SPA central cryptomaria are not younger than Early Imbrian, which is similar to the previous general estimate of 3.88 Ga by Whitten and Head (2015a). In addition, the average albedo and surface roughness of all interpreted cryptomaria are comparable to those of other cryptomaria mapped elsewhere on the Moon (Whitten & Head, 2015a). Consistent with the global spectral investigation of lunar cryptomaria (Whitten & Head, 2015b), the composition of cryptomaria in the SPA basin center is not significantly different from that of the local exposed younger maria (Figure 9).

It is worth noting that the distribution of the SPA central cryptomaria appears to be correlated with the SPA deep structure. Although SPA may not be a “mascon” basin (Trowbridge et al., 2020), there is a large excess of mass under the SPA basin (James et al., 2019). As shown in Figure 8, most identified SPA central cryptomaria occur in the area of overlap between SPACA and mass excess, but the mass excess extends further south right up to the location of the possible SPA peak ring estimated from the ring spacing relationship (Figures 3a and 3b). This supports the interpretation that the surface mare and cryptomare deposits are not the key factors in the formation

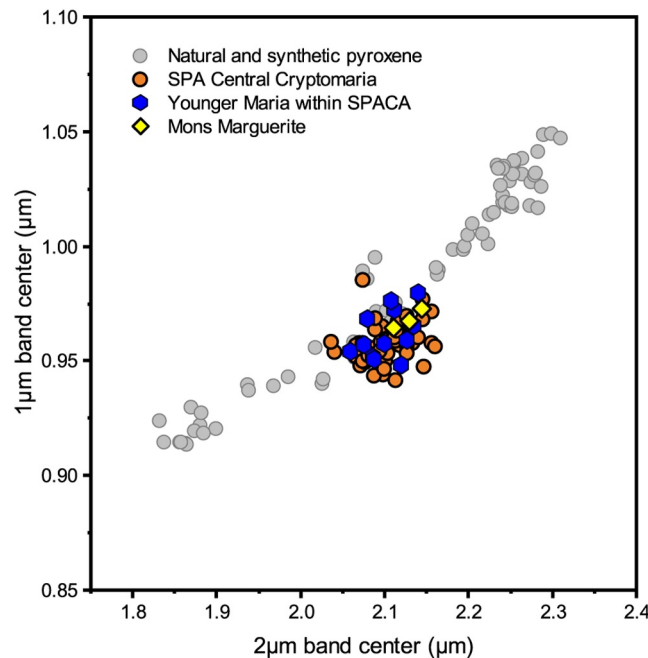


**Figure 9.** Band centers of the South Pole-Aitken (SPA) central cryptomaria, local younger maria and Mons Marguerite. The comparison shows that the composition of cryptomaria in the SPA basin center and Mons Marguerite is not significantly different from that of the local exposed younger maria. The background gray points are from natural and synthetic pyroxene, and the band center values are from Liu et al. (2022), in which the same spectral data processing methods were used as in this paper. The orange points for the SPA central cryptomaria are the same as those labeled “HCP” in Figures S5 and S6 in Supporting Information S1, and the blue points for the local younger maria are the same as those labeled “LM”. The yellow points for Mons Marguerite are calculated from the spectra shown in Figure S7 in Supporting Information S1.

of the SPA mass excess. As James et al. (2019) pointed out, this non-concentric mass anomaly may represent (a) the remnant of the metal core of the SPA impactor or (b) products from the last stage of magma ocean crystallization. This mass anomaly probably indicates the central area of the SPA impact target. The SPA impact resulted in crust thinning, making it easier for basalt to erupt onto the surface (e.g., Head & Wilson, 1992, 2017), though the total volume is less than nearside basins (e.g., Pasckert et al., 2018). Furthermore, this also suggests that the presence of SPA impact melt deposits south of SPACA is plausible.

### 4.3. Mons Marguerite Area

Mons Marguerite (earlier known as “Mafic Mound”), located near the center of the SPA basin, has been previously studied by Moriarty and Pieters (2015). This enigmatic feature is ~75 km across and ~1 km high (Figure 9) and is composed of intermediate-albedo HCP-bearing material. Moriarty and Pieters (2015) evaluated four processes of origin: (a) uplifted mantle, (b) SPA-derived impact melt, (c) a basalt-filled impact crater, or 4) a volcanic construct, and found that none of these individual processes could fully reproduce Mons Marguerite properties. They instead proposed a hybrid origin in which Mons Marguerite is “an edifice formed using magmatic processes induced by the formation and evolution of the SPA impact. This form of non-mare volcanism has not previously been documented on the Moon”. While this interpretation is certainly plausible, the ~75 km across and ~1 km height of the edifice, as well as the large, 32 km diameter perched circular feature, are likely unprecedented volcanic features on the Moon (e.g., Head & Wilson, 2017; Moriarty & Pieters, 2015). In addition, most constructional domes on the Moon (small shield volcanoes) are <20 km in diameter and less than a few hundred meters high, with summit pits less than about 3 km in diameter (Head & Gifford, 1980).

We re-examined Mons Marguerite in the context of our regional analysis and propose two additional candidate interpretations for the higher local topography. First, we compared the morphology and topography of Mons Marguerite (Figures 10a and 10b) with similar plateau-like features found in other mare regions. Comparable plateaus have been recently documented as “mare mesas” in Mare Fecunditatis (Head & Ivanov, 2023; Ivanov et al., 2023) (Figures 10c and 10d), some including superposed circular depressions (craters). These mare mesas have been interpreted to be remnant plateaus of earlier mare material anchored on subsurface topography, with the



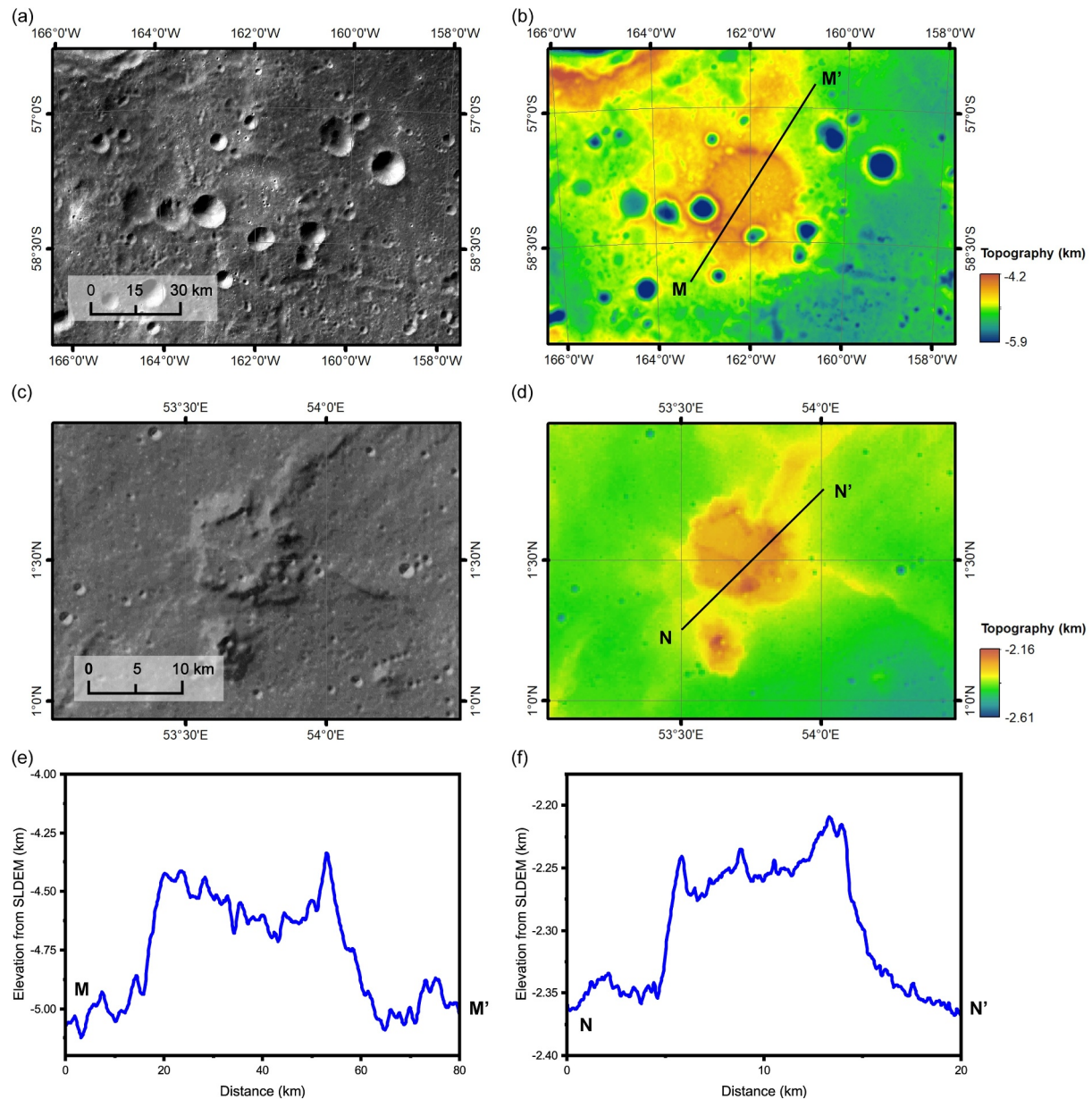


**Figure 10.** Morphological and topographic comparison between Mons Marguerite in panels (a, b) and one mare mesa found in Mare Fecunditatis in panels (c, d) (Ivanov et al., 2023). (a, c) are CE-2 digital orthophoto model images overlain on the shaded relief maps. (b, d) are topographic maps from SLDEM data. (e, f) are the cross sections of MM' (Mons Marguerite) and NN' (Fecunditatis mare mesa).

peripheral maria cooling and solidifying and subsiding to form the steeper mare mesa margins (essentially a type of “mare kipuka”) (Head & Ivanov, 2023; Ivanov et al., 2023). In this scenario, Mons Marguerite formed at a time when local cryptomaria were emplaced. The local area was originally flooded by basalt together with the SPACA cryptomaria documented in this work, and then subsided around an anchor forming a topographic high terrain. Second, ejecta deposits can also create local highs. In this scenario, Mons Marguerite could be in the ejecta blanket of the ghost crater to the east (Figures 7a and 7b), an interpretation supported by its overall very irregular shape and rough surface. A later smaller superposed impact may have formed the nearly circular central summit feature on Mons Marguerite. Subsequent lava flooding may have filled the crater interior (e.g., Figure 7d), mimicking a volcanic constructional plateau (the latter being the model envisioned by Moriarty & Pieters, 2015). Indeed, these two scenarios may also occur in combination. Moreover, as shown in Figure 9 and Figure S7 in

Supporting Information S1, the spectral properties of MM strongly suggest mare basalt affinities, and the similarity in composition between Mons Marguerite and the SPA central cryptomaria supports the idea that Mons Marguerite is likely to be associated with the local cryptomaria rather than SPA impact melt, which is supposed to be LCP-dominated. The HCP-dominated spectral signature of Mons Marguerite is either the basaltic feature of the remnant structure itself or the result of subsequent lava flooding.

After the locally higher terrain formed, the surface of the Mons Marguerite area could be brightened by multiple deposits of crater ejecta, and the central summit formed by an impact crater may be further filled, especially in the second scenario. Indeed, proximal HCP-bearing ejecta, such as from the Bhabha crater, were likely deposited in this area (Petro et al., 2011). In Figure 7a, several pronounced secondaries from distant craters can be observed crossing over Mons Marguerite, such as from the Imbrian-aged Minnaert crater. This relationship also implies that Mons Marguerite has an ancient age. The long, linear, bright ejecta ray (probably from Jackson crater) seen in the OMAT map (Figure 2g) also covers this area, contributing to a further increase in its albedo.

## 5. Implications for Lunar Farside Volcanic Activity and SPA Evolution

Our estimate for the volume of the SPA central cryptomare deposits is at least  $1 \times 10^5 \text{ km}^3$ , representing an  $\sim 2.5$  times increase relative to the previous investigation of the cryptomaria in SPACA (Whitten & Head, 2015a), and at least an  $\sim 0.5\%$  increase in the total volume of global lunar mare deposits ( $1 \times 10^7 \text{ km}^3$ ; Head, 1975) and lunar cryptomare deposits ( $1 \times 10^6 \text{ km}^3$ ; Whitten & Head, 2015a). Based on the findings of Yingst and Head (1997), this SPA central cryptomaria volume is about 65% more than the volume of verified mare deposits in the SPA basin, and about 16 times greater than their verified mare deposits in the basin interior SPACA area. When considering the estimates provided by Pasckert et al. (2018), these values increase by 8 and 72 times, respectively. It is also  $\sim 10$  times the volume of Orientale basin interior mare deposits ( $10,440 \text{ km}^3$ ; Whitten et al., 2011). If we assume that cryptomaria are present where all HCP compositions occur within the basin central areas ( $\sim 1.6 \times 10^5 \text{ km}^2$ , Figure 8), with an expected average thickness of 1.5 km, this provides the largest volume for the SPA central cryptomare deposits ( $\sim 2.4 \times 10^5 \text{ km}^3$ ), and would account for  $\sim 1.8\%$  of the total lunar mare and cryptomare deposit volume. This maximum mare basalt volume estimate, when compared to the volume of nearside maria basins, is comparable to the volume of Mare Tranquillitatis ( $\sim 2.6 \times 10^5 \text{ km}^3$ ; Head, 1975). Therefore, even though our analysis has greatly increased the total volume of mare and cryptomare deposits on the lunar farside, there remains a considerable asymmetry in the distribution and abundance of mare deposits between the lunar nearside and farside. As clearly shown in Figure 11a, the SPA basin remains significantly underfilled relative to the nearside mascon basins.

Many researchers have pointed out that the lunar mare deposit nearside/farside hemispherical asymmetry is closely related to the difference in crustal thickness (e.g., Head & Wilson, 1992, 2017). On the lunar farside, the crust is generally thicker than the nearside, probably averaging  $\sim 50 \text{ km}$  (Figure 3 in Wiczorek et al., 2013), compared to the nearside average value ( $\sim 30 \text{ km}$ ). In this scenario (Head & Wilson, 1992), more dikes would stall within the crust, extruding only in the deepest basins and thinnest crust, such as the SPA basin interior. If this hypothesis is correct, it would also predict the presence of significant volumes of cryptomaria dating from the earlier impact-basin dominated era, including that observed in SPA (Whitten & Head, 2015a, 2015b).

Further evaluation of the multiple nearside-farside asymmetries can be made in terms of variable thermal anomalies below the newly formed SPA basin, some of which may have resulted from a potential paucity of heat-producing elements. Zhong et al. (2000) proposed that this could be the result of possible degree-1 mantle convection in early lunar history. Recent numerical simulations suggested that the giant SPA impact event could have served to transfer a farside basal crust KREEP layer to the nearside through hemisphere-scale mantle convection (Jones et al., 2022; Zhang et al., 2022). The excavation of the SPA impact event may have also removed the heat-producing elements (Moriarty et al., 2021a). These factors may also contribute to the observed smaller farside mare abundances and locations.

This work also further supports that the SPA basin can be placed into the population of virtually all other impact basins on the Moon in having been filled with voluminous and continuous post-basin-formation mare deposits (Figure 11b). In addition to the cryptomaria and maria, crater and basin ejecta deposits from both inside the basin (e.g., the Apollo basin and many other smaller craters) and outside the basin (e.g., the Orientale basin) have also contributed to the SPA interior infilling (e.g., Guo et al., 2018; Meyer et al., 2020). Specifically, substantial



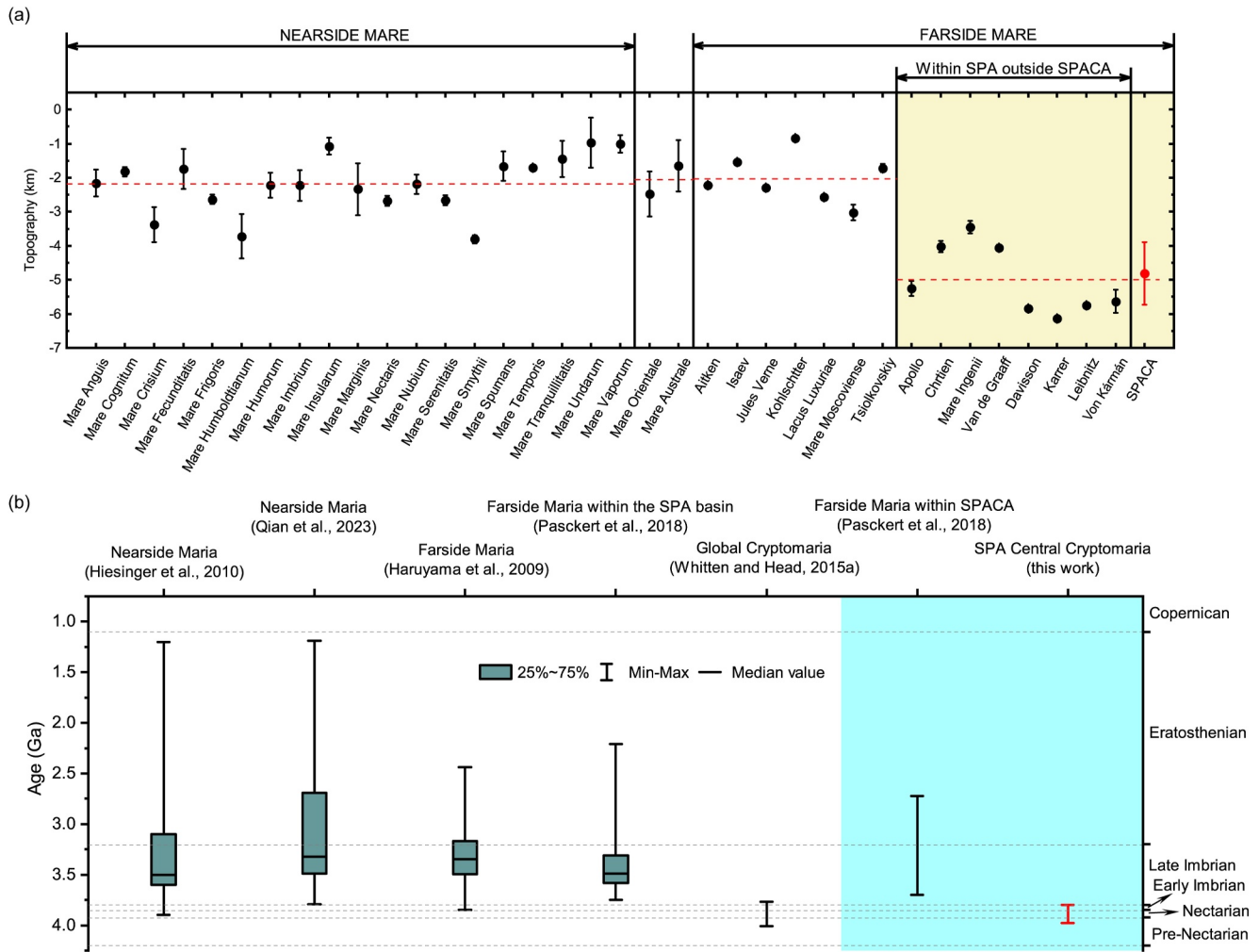


**Figure 11.** Average topography and ages of lunar global mare/cryptomare deposits and SPACA. The topographic values in panel (a) are obtained by calculating the average value in each mare unit using the mare boundaries from Nelson et al. (2014). The maria/cryptomaria within the South Pole-Aitken (SPA) basin are highlighted by a light yellow background in (a). It is obvious that SPA remains significantly underfilled relative to other basins on the Moon. (b) shows the ages of global mare/cryptomare deposits measured by several studies (Haruyama et al., 2009; Hiesinger et al., 2010; Pasckert et al., 2018; Qian et al., 2023; Whitten & Head, 2015a). The maria and the cryptomaria within the SPACA are highlighted by a light cyan background showing that the post-basin-formation cryptomare/mare deposits are continuous in the SPA basin center.

Apollo ejecta have significantly aided in shaping the interior SPA topography and terrain. Consequently, we reconstructed the sequence of crustal stratigraphy of the central SPA region as follows (Figure 12): from the bottom of the diagram we show (a) Th-rich LCP-bearing upper differentiated SPA impact-melt sheet; (b) a large number of impact events modified the SPA basin interior, forming dense impact craters and basins within the SPA basin, and excavating the preexisting SPA impact melt and ejecta; (c) unvalidated but possible existence of the pre-Apollo basin cryptomaria; (d) thick LCP-bearing Apollo ejecta deposits and other ejecta deposits; (e) emplacement of thick ancient mare deposits (now cryptomaria) then partly modified and partly buried by (f) proximal ejecta from nearby craters and distal ejecta from Orientale and other large basins, eventually forming the cryptomaria observed today; (g) emplacement of numerous individual patches of younger mare deposits with low albedo surfaces.

## 6. Conclusions

We investigated the nature and origin of the SPACA region in the context of the geological history, topography, morphology and mineralogy of the SPA basin interior and vicinity and conclude that:

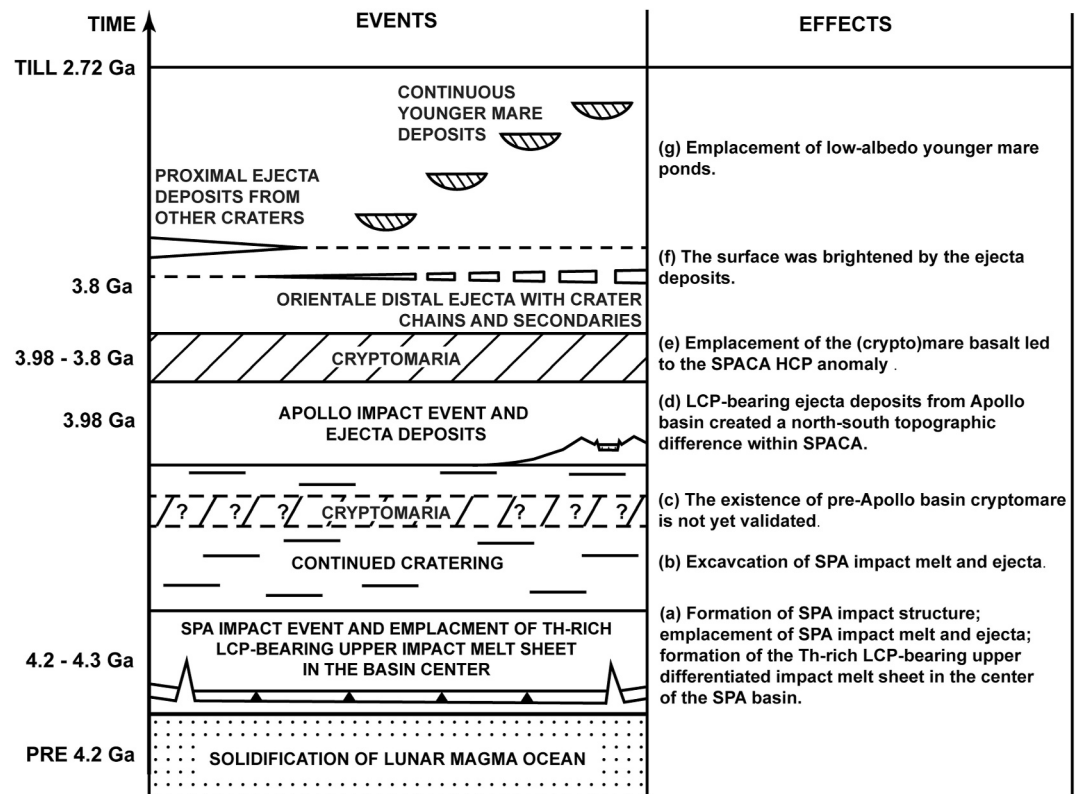


**Figure 12.** The timeline of the events occurring in the South Pole-Aitken (SPA) basin center and their effects. The age of the SPA impact event is from Hiesinger et al. (2012). The age of the Apollo impact event is from Ivanov et al. (2018). The age of the Orientale basin is from Yue et al. (2020). The age range of younger mare deposits occurring within the SPACA is from Pasckert et al. (2018).

1. The central region of the SPA basin has experienced widespread post-basin formation resurfacing events. We interpret the SPACA to have originated from more extensive cryptomaria deposits in the basin center rather than a differentiated impact melt sheet. The extent of the SPACA appears much smaller than the predicted SPA impact melt sheet, which we may observe in the area south of SPACA.
2. Our detailed analysis suggests that the relative ages of the SPA central cryptomaria are not younger than Early Imbrian (Figure 11b). The interior of the SPA basin center is filled with cryptomaria exceeding 1 km in thickness, with an areal extent of at least  $8.7 \times 10^4 \text{ km}^2$ , corresponding to a minimum volume estimate of  $\sim 1 \times 10^5 \text{ km}^3$ . This represents at least a 0.5% increase in the total volume of global lunar mare and cryptomare deposits. Nevertheless, the difference in the areal distribution and abundance of mare basalts between the lunar nearside and farside still clearly exists. Crustal thickness variations may account for the concentration of farside maria in the SPA basin, yet it remains underfilled.
3. We show that, in a manner similar to the nearside basins, the SPA basin was a site of voluminous and continuous post-basin formation mare fill. The SPACA terrain is largely formed by emplacement of mare basalt deposits in a sequential fashion subsequent to the formation of the SPA basin, and interleaved with impact crater deposits, derived largely from within the SPA basin. These sequentially accumulating mare basalt deposits were eventually modified and partially buried by ejecta deposits from nearby and distant craters and basins, adding high-albedo ejecta to mix with their surfaces and form the moderate-albedo cryptomaria, as is seen in most other cryptomaria on the Moon (Whitten & Head, 2015a). Continued eruption of mare basalt magma in the post-Orientale basin period formed multiple patches of mare basalts whose albedo and spectral affinities are similar to those of nearside maria. The presence and abundance of post-SPA basin and pre-Apollo-basin mare volcanic activity is currently unknown.
4. We find no compelling reason to call on special SPA impact-induced petrogenetic circumstances to account for the intermediate albedo of the SPACA cryptomaria relative to the subsequent, geographically co-located younger SPA mare deposits (e.g., Moriarty & Pieters, 2015).

5. We provide an alternative view of the formation of the Bhabha/Mons Marguerite area by interpreting the localized topography of Mons Marguerite as an old impact crater superposed on a possible mare mesa or on an ejecta blanket, and the circular feature was then filled with more volcanic materials and brightened by additional highland crater ejecta deposits. In addition, we interpret the distinctive composition observed on the wall and ejecta of Bhabha as due to the excavation of local buried cryptomaria.
6. Despite our finding of revisit in volume of cryptomare-mare in the SPA basin interior, the SPA contains much less total mare material than that observed in nearside mare mascon basins. The SPA basin interior remains anomalous in that it is characterized by the thinnest crust and the lowest topography on the Moon.

As the largest and oldest impact structure on the Moon, the SPA basin is among the highest priority sites for future lunar exploration and lunar sample return. Chang'E-6, China's next sample return mission scheduled to launch in May 2024, will land within the SPA basin (Zeng et al., 2023). One of the candidate landing areas of Chang'E-6 mission is the cryptomare south of the Apollo basin (Region I in this work). In addition to the China's Chang'E-6 mission, a potential NASA mission, *Endurance* (Keane et al., 2022), is designed to traverse the entire basin through the basin center, and also return relevant samples. Samples collected by these missions from the central cryptomaria would be critical ground truth for assessing the early thermal history of the lunar farside, and their comparison with Apollo/Luna/Chang'E samples collected from the lunar nearside would also help to unravel the causes of the hemispherical asymmetry of mare deposits. Our findings in this work can provide important guidance for these missions and can be tested by future returned samples.

## Data Availability Statement

All raw data used in this work are available at the NASA Planetary Data System (PDS) or China's Lunar and Planetary Data Release System. Specifically, the SLDEM2015 can be downloaded from Robinson (2011). The MI data used in this work can be accessed by searching "SLN-L-MI-5-MAP-V3.0" at [https://darts.isas.jaxa.jp/planet/pdap/selene/product\\_search.html](https://darts.isas.jaxa.jp/planet/pdap/selene/product_search.html). The M<sup>3</sup> spectral data are available at Malaret (2011). The half-degree Th abundance map derived from LP GRS is accessible from Prettyman (2021). LOLA albedo map can be obtained from Robinson (2011). The crustal thickness models derived from GRAIL data are archived at the Zenodo repository (Wieczorek, 2012). The 5–20 km crater data, the >20 km crater data and the LOLA surface roughness map were derived from Povilaitis et al. (2018), Head et al. (2010) and Kreslavsky et al. (2013), respectively. The CE-2 DOM data is accessible from China's Lunar and Planet Exploration Program Ground Application System (China National Space Administration, 2020) under the CE-2 label. The locations and band parameters of the M<sup>3</sup> spectra extracted in this study are provided in the Table S1 in Supporting Information S1. The areal extents of the SPA central cryptomaria shown in Figure 8 are archived at the Zenodo repository (Wang et al., 2023).

## Acknowledgments

We gratefully acknowledge very useful and informative discussions with Dr. Carle Pieters. We thank Dr. Jennifer Whitten for providing us with the boundaries of the global cryptomaria. This work was supported by the National Natural Science Foundation of China (NSFC) (Grant 12373068 and 42371384). X.W. is also supported by International Cooperation Training Program from the University of Chinese Academy of Sciences.

## References

- Antonenko, I., Head, J. W., Mustard, J. F., & Ray Hawke, B. (1995). Criteria for the detection of lunar cryptomaria. *Earth, Moon, and Planets*, 69(2), 141–172. <https://doi.org/10.1007/BF00613096>
- Baker, D. M., & Head, J. W. (2015). Constraints on the depths of origin of peak rings on the Moon from Moon Mineralogy Mapper data. *Icarus*, 258, 164–180. <https://doi.org/10.1016/j.icarus.2015.06.013>
- Baker, D. M., Head, J. W., Neumann, G. A., Smith, D. E., & Zuber, M. T. (2012). The transition from complex craters to multi-ring basins on the Moon: Quantitative geometric properties from Lunar Reconnaissance Orbiter Lunar Orbiter Laser Altimeter (LOLA) data. *Journal of Geophysical Research*, 117(E12). <https://doi.org/10.1029/2011JE004021>
- Barabashov, N. P. (Ed.) (1961). *An atlas of the Moon's far side: The Lunik III reconnaissance*. Interscience Publishers.
- Barker, M. K., Mazarico, E., Neumann, G. A., Zuber, M. T., Haruyama, J., & Smith, D. E. (2016). A new lunar digital elevation model from the Lunar Orbiter Laser Altimeter and SELENE Terrain Camera. *Icarus*, 273, 346–355. <https://doi.org/10.1016/j.icarus.2015.07.039>
- China National Space Administration. (2020). Ground research and application system of China's lunar and planetary exploration program. Chang'E-2 global digital orthophoto model dataset. <https://doi.org/10.12350/CLPDS.GRAS.CE2.DOM-50m.vA>
- Chuang, F. C., Whitten, J. L., Domingue, D. L., Watkins, R. N., Jolliff, B. L., Valencia, S. N., & Moriarty, D. P. (2022). Analysis of surface roughness in mare, cryptomare and non-mare terrains, lunar South Pole-Aitken basin. In *53rd Lunar and Planetary Science Conference*. Abstract # 1449.
- Croft, S. K. (1985). The scaling of complex craters. *Journal of Geophysical Research*, 90(S02), C828–C842. <https://doi.org/10.1029/JB090iS02p0C828>
- Fassett, C. I., Head, J. W., Smith, D. E., Zuber, M. T., & Neumann, G. A. (2011). Thickness of proximal ejecta from the Orientale Basin from Lunar Orbiter Laser Altimeter (LOLA) data: Implications for multi-ring basin formation. *Geophysical Research Letters*, 38(17). <https://doi.org/10.1029/2011GL048502>
- Garrick-Bethell, I., & Zuber, M. T. (2009). Elliptical structure of the lunar South Pole-Aitken basin. *Icarus*, 204(2), 399–408. <https://doi.org/10.1016/j.icarus.2009.05.032>



- Guo, D., Liu, J., Head, J. W. III., & Kreslavsky, M. A. (2018). Lunar Orientale impact basin secondary craters: Spatial distribution, size-frequency distribution, and estimation of fragment size. *Journal of Geophysical Research: Planets*, 123(6), 1344–1367. <https://doi.org/10.1029/2017JE005446>
- Haruyama, J., Ohtake, M., Matsunaga, T., Morota, T., Honda, C., Yokota, Y., et al. (2009). Long-lived volcanism on the lunar farside revealed by SELENE Terrain Camera. *Science*, 323(5916), 905–908. <https://doi.org/10.1126/science.1163382>
- Head, J. W. (1974). Orientale multi-ringed basin interior and implications for the petrogenesis of lunar highland samples. *The Moon*, 11(3–4), 327–356. <https://doi.org/10.1007/BF00589168>
- Head, J. W. (1975). Lunar mare deposits: Areas, volumes, sequence, and implication for melting in source areas. *Origins of Mare Basalts and their Implications for Lunar Evolution*, 234, 66.
- Head, J. W. (1976). Lunar volcanism in space and time. *Reviews of Geophysics*, 14(2), 265–300. <https://doi.org/10.1029/RG014i002p00265>
- Head, J. W. (2010). Transition from complex craters to multi-ringed basins on terrestrial planetary bodies: Scale-dependent role of the expanding melt cavity and progressive interaction with the displaced zone. *Geophysical Research Letters*, 37(2). <https://doi.org/10.1029/2009GL041790>
- Head, J. W., & Gifford, A. (1980). Lunar mare domes: Classification and modes of origin. *The Moon and the Planets*, 22(2), 235–258. <https://doi.org/10.1007/BF00898434>
- Head, J. W., & Ivanov, M. A. (2023). Mare mesas in mare Fecunditatis: Characteristics of a newly documented class of mare volcanic feature. In *14th Moscow Solar System Symposium*.
- Head, J. W., & Wilson, L. (1992). Lunar mare volcanism: Stratigraphy, eruption conditions, and the evolution of secondary crusts. *Geochimica et Cosmochimica Acta*, 56(6), 2155–2175. [https://doi.org/10.1016/0016-7037\(92\)90183-J](https://doi.org/10.1016/0016-7037(92)90183-J)
- Head, J. W., & Wilson, L. (2017). Generation, ascent and eruption of magma on the Moon: New insights into source depths, magma supply, intrusions and effusive/explosive eruptions (Part 2: Predicted emplacement processes and observations). *Icarus*, 283, 176–223. <https://doi.org/10.1016/j.icarus.2016.05.031>
- Head, J. W. III., Fassett, C. I., Kadish, S. J., Smith, D. E., Zuber, M. T., Neumann, G. A., & Mazarico, E. (2010). Global distribution of large lunar craters: Implications for resurfacing and impactor populations. *Science*, 329(5998), 1504–1507. <https://doi.org/10.1126/science.1195050>
- Hiesinger, H., Head, J. W. III, Wolf, U., Jaumann, R., & Neukum, G. (2010). Ages and stratigraphy of lunar mare basalts in Mare Frigoris and other nearside maria based on crater size-frequency distribution measurements. *Journal of Geophysical Research*, 115(E3). <https://doi.org/10.1029/2009JE003380>
- Hiesinger, H., van der Bogert, C. H., Pasckert, J. H., Schmedemann, N., Robinson, M. S., Jolliff, B., & Petro, N. (2012). New crater size-frequency distribution measurements of the South Pole-Aitken basin. In *43rd Annual Lunar And Planetary Science Conference*. Abstract # 2863.
- Hurwitz, D. M., & Kring, D. A. (2014). Differentiation of the South Pole-Aitken basin impact melt sheet: Implications for lunar exploration. *Journal of Geophysical Research: Planets*, 119(6), 1110–1133. <https://doi.org/10.1002/2013JE004530>
- Ivanov, M. A., Head, J. W., & Hiesinger, H. (2023). New insights into the regional and local geological context of the Luna 16 landing site. *Icarus*, 400, 115579. <https://doi.org/10.1016/j.icarus.2023.115579>
- Ivanov, M. A., Hiesinger, H., Van Der Bogert, C. H., Orgel, C., Pasckert, J. H., & Head, J. W. (2018). Geologic history of the northern portion of the South Pole-Aitken basin on the Moon. *Journal of Geophysical Research: Planets*, 123(10), 2585–2612. <https://doi.org/10.1029/2018JE005590>
- Izquierdo, K., Sori, M. M., Checketts, B., Hampton, I., Johnson, B. C., & Soderblom, J. M. (2024). Global distribution and volume of cryptomare and visible Mare on the Moon from gravity and dark halo craters. *Journal of Geophysical Research: Planets*, 129(2), e2023JE007867. <https://doi.org/10.1029/2023JE007867>
- James, P. B., Smith, D. E., Byrne, P. K., Kendall, J. D., Melosh, H. J., & Zuber, M. T. (2019). Deep structure of the lunar South Pole-Aitken basin. *Geophysical Research Letters*, 46(10), 5100–5106. <https://doi.org/10.1029/2019GL082252>
- Johnson, B. C., Blair, D. M., Collins, G. S., Melosh, H. J., Freed, A. M., Taylor, G. J., et al. (2016). Formation of the Orientale lunar multiring basin. *Science*, 354(6311), 441–444. <https://doi.org/10.1126/science.aag0518>
- Jones, M. J., Evans, A. J., Johnson, B. C., Weller, M. B., Andrews-Hanna, J. C., Tikoo, S. M., & Keane, J. T. (2022). A South Pole-Aitken impact origin of the lunar compositional asymmetry. *Science Advances*, 8(14), eabm8475. <https://doi.org/10.1126/sciadv.abm8475>
- Keane, J. T., Tikoo, S. M., Elliott, J. O., Clark, P. E., Denevi, B. W., Evans, A. J., et al. (2022). Endurance: Lunar south Pole-Aitken basin traverse and sample return rover. In *2022 Annual Meeting of the Lunar Exploration Analysis Group*. Abstract # 5031.
- Kreslavsky, M. A., Head, J. W., Neumann, G. A., Rosenburg, M. A., Aharonson, O., Smith, D. E., & Zuber, M. T. (2013). Lunar topographic roughness maps from Lunar Orbiter Laser Altimeter (LOLA) data: Scale dependence and correlation with geologic features and units. *Icarus*, 226(1), 52–66. <https://doi.org/10.1016/j.icarus.2013.04.027>
- Lawrence, D. J., Elphic, R. C., Feldman, W. C., Prettyman, T. H., Gasnault, O., & Maurice, S. (2003). Small-area thorium features on the lunar surface. *Journal of Geophysical Research*, 108(E9). <https://doi.org/10.1029/2003JE002050>
- Lawrence, D. J., Feldman, W. C., Elphic, R. C., Little, R. C., Prettyman, T. H., Maurice, S., et al. (2002). Iron abundances on the lunar surface as measured by the Lunar Prospector gamma-ray and neutron spectrometers. *Journal of Geophysical Research*, 107(E12), 13–21. <https://doi.org/10.1029/2001JE001530>
- Lemelin, M., Lucey, P. G., Miljković, K., Gaddis, L. R., Hare, T., & Ohtake, M. (2019). The compositions of the lunar crust and upper mantle: Spectral analysis of the inner rings of lunar impact basins. *Planetary and Space Science*, 165, 230–243. <https://doi.org/10.1016/j.pss.2018.10.003>
- Lemelin, M., Lucey, P. G., Neumann, G. A., Mazarico, E. M., Barker, M. K., Kakazu, A., et al. (2016). Improved calibration of reflectance data from the LRO Lunar Orbiter Laser Altimeter (LOLA) and implications for space weathering. *Icarus*, 273, 315–328. <https://doi.org/10.1016/j.icarus.2016.02.006>
- Lemelin, M., Lucey, P. G., Song, E., & Taylor, G. J. (2015). Lunar central peak mineralogy and iron content using the Kaguya Multiband Imager: Reassessment of the compositional structure of the lunar crust. *Journal of Geophysical Research: Planets*, 120(5), 869–887. <https://doi.org/10.1002/2014JE004778>
- Li, C., Liu, J., Ren, X., Yan, W., Zuo, W., Mu, L., et al. (2018). Lunar global high-precision terrain reconstruction based on Chang'E-2 stereo images. *Geomatics and Information Science of Wuhan University*, 43(4), 485–495. <https://doi.org/10.13203/j.whugis.20170400>
- Liu, D., Wang, X., Liu, J., Liu, B., Ren, X., Chen, Y., et al. (2022). Spectral interpretation of late-stage mare basalt mineralogy unveiled by Chang'E-5 samples. *Nature Communications*, 13(1), 5965. <https://doi.org/10.1038/s41467-022-33670-6>
- Malaret, E. (2011). CH1-ORB Moon M3 4 L2 reflectance near-IR spectral IMGS V1.0 [Dataset]. *NASA Planetary Data System*. <https://doi.org/10.17189/1520414>
- McGetchin, T. R., Settle, M., & Head, J. W. (1973). Radial thickness variation in impact crater ejecta: Implications for lunar basin deposits. *Earth and Planetary Science Letters*, 20(2), 226–236. [https://doi.org/10.1016/0012-821X\(73\)90162-3](https://doi.org/10.1016/0012-821X(73)90162-3)
- Melosh, H. J. (1989). *Impact cratering: A geologic process*. Oxford University Press; Oxford: Clarendon Press.

- Melosh, H. J., Kendall, J., Horgan, B., Johnson, B. C., Bowling, T., Lucey, P. G., & Taylor, G. J. (2017). South Pole–Aitken basin ejecta reveal the Moon's upper mantle. *Geology*, 45(12), 1063–1066. <https://doi.org/10.1130/G39375.1>
- Meyer, H. M., Denevi, B. W., Robinson, M. S., & Boyd, A. K. (2020). The global distribution of lunar light plains from the lunar reconnaissance orbiter camera. *Journal of Geophysical Research: Planets*, 125(1), e2019JE006073. <https://doi.org/10.1029/2019JE006073>
- Moriarty, D. P. III., Milla, M., Watkins, R. N., Domingue, D. L., Valencia, S. N., Whitten, J., et al. (2022). A preliminary evaluation of resurfacing scenarios across the South Pole-Aitken basin interior from a mineralogical assessment of craters. In *53rd Lunar and Planetary Science Conference*. Abstract # 2386.
- Moriarty, D. P. III., Dygert, N., Valencia, S. N., Watkins, R. N., & Petro, N. E. (2021). The search for lunar mantle rocks exposed on the surface of the Moon. *Nature Communications*, 12(1), 4659. <https://doi.org/10.1038/s41467-021-24626-3>
- Moriarty, D. P. III., & Pieters, C. M. (2018). The character of South Pole-Aitken Basin: Patterns of surface and subsurface composition. *Journal of Geophysical Research: Planets*, 123(3), 729–747. <https://doi.org/10.1002/2017JE005364>
- Moriarty, D. P. III., & Pieters, C. M. (2015). The nature and origin of mafic mound in the South Pole-Aitken Basin. *Geophysical Research Letters*, 42(19), 7907–7915. <https://doi.org/10.1002/2015GL065718>
- Moriarty, D. P. III., Watkins, R. N., Valencia, S. N., Kendall, J. D., Evans, A. J., Dygert, N., & Petro, N. E. (2021a). Evidence for a stratified upper mantle preserved within the South Pole-Aitken basin. *Journal of Geophysical Research: Planets*, 126(1), e2020JE006589. <https://doi.org/10.1029/2020JE006589>
- Nelson, D. M., Koeber, S. D., Daud, K., Robinson, M. S., Watters, T. R., Banks, M. E., & Williams, N. R. (2014). Mapping lunar Maria extents and lobate scarps using LROC image products. In *45th Lunar and Planetary Science Conference*. Abstract #2861.
- Neukum, G. (1983). Meteoriten bombardement Und Datierung Planetarer Oberflächen Habilitation Thesis for Faculty Membership. Univ. Of Munich. (English Translation, 1984: Meteorite Bombardment and Dating of Planetary Surfaces). Habilitation Thesis. University München, Munich, Germany (p. 186).
- Neukum, G., Ivanov, B. A., & Hartmann, W. K. (2001). Cratering records in the inner solar system in relation to the lunar reference system. In *Chronology and evolution of Mars: Proceedings of an ISSI Workshop, 10-14 April 2000* (pp. 55–86). Springer Netherlands.
- Noether, G. E. (1978). A brief survey of nonparametric statistics. In R. V. Hogg (Ed.), *Studies in statistics* (pp. 39–65). Mathematical Association of America.
- Ogawa, Y., Matsunaga, T., Nakamura, R., Saiki, K., Ohtake, M., Hiroi, T., et al. (2011). The widespread occurrence of high-calcium pyroxene in bright-ray craters on the Moon and implications for lunar-crust composition. *Geophysical Research Letters*, 38(17). <https://doi.org/10.1029/2011GL048569>
- Ohtake, M., Haruyama, J., Matsunaga, T., Yokota, Y., Morota, T., & Honda, C., & LISM team. (2008). Performance and scientific objectives of the SELENE (KAGUYA) Multiband imager. *Earth Planets and Space*, 60(4), 257–264. <https://doi.org/10.1186/BF03352789>
- Ohtake, M., Uemoto, K., Yokota, Y., Morota, T., Yamamoto, S., Nakamura, R., et al. (2014). Geologic structure generated by large-impact basin formation observed at the South Pole-Aitken basin on the Moon. *Geophysical Research Letters*, 41(8), 2738–2745. <https://doi.org/10.1002/2014GL059478>
- Pasckert, J. H., Hiesinger, H., & van der Bogert, C. H. (2018). Lunar farside volcanism in and around the South Pole–Aitken basin. *Icarus*, 299, 538–562. <https://doi.org/10.1016/j.icarus.2017.07.023>
- Petro, N. E. (2011). Volume of impact melt generated by the formation of the South Pole-Aitken basin. In *2011 Annual Meeting of the Lunar Exploration Analysis Group*. Abstract # 2051.
- Petro, N. E., Mest, S. C., & Teich, Y. (2011). Geomorphic terrains and evidence for ancient volcanism within northeastern South Pole-Aitken basin. *Special Papers - Geological Society of America*, 477, 129–140. <https://doi.org/10.1130/2011.2477/06>
- Petro, N. E., & Pieters, C. M. (2004). Surviving the heavy bombardment: Ancient material at the surface of south Pole-Aitken Basin. *Journal of Geophysical Research*, 109(E6). <https://doi.org/10.1029/2003JE002182>
- Pieters, C. M., Boardman, J., Buratti, B., Chatterjee, A., Clark, R., Glavich, T., et al. (2009). The Moon mineralogy mapper (M<sup>3</sup>) on chandrayaan-1. *Current Science*, 500–505. Retrieved from <http://www.jstor.org/stable/24105459>
- Pieters, C. M., Head, J. W. III., Gaddis, L., Jolliff, B., & Duke, M. (2001). Rock types of South Pole-Aitken basin and extent of basaltic volcanism. *Journal of Geophysical Research*, 106(E11), 28001–28022. <https://doi.org/10.1029/2000JE001414>
- Pike, R. J. (1974). Ejecta from large craters on the Moon: Comments on the geometric model of McGetchin et al. *Earth and Planetary Science Letters*, 23(3), 265–271. [https://doi.org/10.1016/0012-821X\(74\)90114-9](https://doi.org/10.1016/0012-821X(74)90114-9)
- Pike, R. J. (1977). Apparent depth/apparent diameter relation for lunar craters. *8th Lunar Science Conference*, 8, 3427–3436.
- Pike, R. J., & Spudis, P. D. (1987). Basin-Ring spacing on the Moon, Mercury, and Mars. *Earth, Moon, and Planets*, 39(2), 129–194. <https://doi.org/10.1007/BF00054060>
- Poehler, C. M., Ivanov, M. A., van der Bogert, C. H., Hiesinger, H., Iqbal, W., Pasckert, J. H., et al. (2020). The lunar south Pole-Aitken Basin region: A new geological map. In *Europlanet Science Congress 2020* (Vol. 14). EPSC2020-600. <https://doi.org/10.5194/epsc2020-600>
- Potter, R. W., Collins, G. S., Kiefer, W. S., McGovern, P. J., & Kring, D. A. (2012). Constraining the size of the South Pole-Aitken basin impact. *Icarus*, 220(2), 730–743. <https://doi.org/10.1016/j.icarus.2012.05.032>
- Povilaitis, R. Z., Robinson, M. S., Van der Bogert, C. H., Hiesinger, H., Meyer, H. M., & Ostrach, L. R. (2018). Crater density differences: Exploring regional resurfacing, secondary crater populations, and crater saturation equilibrium on the Moon. *Planetary and Space Science*, 162, 41–51. <https://doi.org/10.1016/j.pss.2017.05.006>
- Prettyman, T. H. (2021). Lunar prospector GRS elemental abundance bundle. *NASA Planetary Data System*. <https://doi.org/10.17189/1519384>
- Qian, Y., She, Z., He, Q., Xiao, L., Wang, Z., Head, J. W., et al. (2023). Mineralogy and chronology of the young mare volcanism in the Procellarum-KREEP-Terrane. *Nature Astronomy*, 7(3), 287–297. <https://doi.org/10.1038/s41550-022-01862-1>
- Robinson, M. (2011). Lro Moon LROC 5 RDR V1.0 [Dataset]. *NASA Planetary Data System*. <https://doi.org/10.17189/1520341>
- Savitzky, A., & Golay, M. J. (1964). Smoothing and differentiation of data by simplified least squares procedures. *Analytical Chemistry*, 36(8), 1627–1639. <https://doi.org/10.1021/ac60214a047>
- Schultz, P. H., & Spudis, P. D. (1983). Beginning and end of lunar mare volcanism. *Nature*, 302(5905), 233–236. <https://doi.org/10.1038/302233a0>
- Sharpton, V. L. (2014). Outcrops on lunar crater rims: Implications for rim construction mechanisms, ejecta volumes and excavation depths. *Journal of Geophysical Research: Planets*, 119(1), 154–168. <https://doi.org/10.1002/2013JE004523>
- Spudis, P. D., Gillis, J. J., & Reisse, R. A. (1994). Ancient multiring basins on the Moon revealed by Clementine laser altimetry. *Science*, 266(5192), 1848–1851. <https://doi.org/10.1126/science.266.5192.184>
- Spudis, P. D., Hawke, B. R., & Lucey, P. (1984). Composition of Orientale basin deposits and implications for the lunar basin-forming process. *Journal of Geophysical Research*, 89(S01), C197–C210. <https://doi.org/10.1029/JB089iS01p0C197>

- Trowbridge, A. J., Johnson, B. C., Freed, A. M., & Melosh, H. J. (2020). Why the lunar South Pole-Aitken Basin is not a mascon. *Icarus*, 352, 113995. <https://doi.org/10.1016/j.icarus.2020.113995>
- Uemoto, K., Ohtake, M., Haruyama, J., Matsunaga, T., Yamamoto, S., Nakamura, R., et al. (2017). Evidence of impact melt sheet differentiation of the lunar South Pole-Aitken basin. *Journal of Geophysical Research: Planets*, 122(8), 1672–1686. <https://doi.org/10.1002/2016JE005209>
- Vaughan, W. M., & Head, J. W. (2014). Impact melt differentiation in the South Pole-Aitken basin: Some observations and speculations. *Planetary and Space Science*, 91, 101–106. <https://doi.org/10.1016/j.pss.2013.11.010>
- Wang, X., Head, J. W., Chen, Y., Zhao, F., Kreslavsky, M. A., Wilson, L., et al. (2023). Areal extents of the SPA central cryptomaria (Version 1.0) [Dataset]. *Zenodo*. <https://doi.org/10.5281/ZENODO.8435503>
- Whitten, J., & Head, J. W. (2015a). Lunar cryptomaria: Mineralogy and composition of ancient volcanic deposits. *Planetary and Space Science*, 106, 67–81. <https://doi.org/10.1016/j.pss.2014.11.027>
- Whitten, J. L., & Head, J. W. (2015b). Lunar cryptomaria: Physical characteristics, distribution, and implications for ancient volcanism. *Icarus*, 247, 150–171. <https://doi.org/10.1016/j.icarus.2014.09.031>
- Whitten, J., Head, J. W., Staid, M., Pieters, C. M., Mustard, J., Clark, R., et al. (2011). Lunar mare deposits associated with the Orientale impact basin: New insights into mineralogy, history, mode of emplacement, and relation to Orientale Basin evolution from Moon Mineralogy Mapper (M3) data from Chandrayaan-1. *Journal of Geophysical Research*, 116(E6), E00G09. <https://doi.org/10.1029/2010JE003736>
- Whitten, J. L., & Head, J. W. III. (2013). Detecting volcanic resurfacing of heavily cratered terrain: Flooding simulations on the Moon using Lunar Orbiter Laser Altimeter (LOLA) data. *Planetary and Space Science*, 85, 24–37. <https://doi.org/10.1016/j.pss.2013.05.013>
- Wieczorek, M. (2012). GRAIL crustal thickness archive [Dataset]. *Zenodo*. <https://doi.org/10.5281/zenodo.997347>
- Wieczorek, M. A., Neumann, G. A., Nimmo, F., Kiefer, W. S., Taylor, G. J., Melosh, H. J., et al. (2013). The crust of the Moon as seen by GRAIL. *Science*, 339(6120), 671–675. <https://doi.org/10.1126/science.1231530>
- Wu, B., Wang, Y., Werner, S. C., Prieur, N. C., & Xiao, Z. (2022). A global analysis of crater depth/diameter ratios on the Moon. *Geophysical Research Letters*, 49(20), e2022GL100886. <https://doi.org/10.1029/2022GL100886>
- Xie, M., & Zhu, M. H. (2016). Estimates of primary ejecta and local material for the Orientale basin: Implications for the formation and ballistic sedimentation of multi-ring basins. *Earth and Planetary Science Letters*, 440, 71–80. <https://doi.org/10.1016/j.epsl.2016.02.012>
- Xu, L., Zhang, X., Qiao, L., & Lai, J. (2021). Evaluating the thickness and stratigraphy of ejecta materials at the Chang'E-4 landing site. *The Astronomical Journal*, 162(1), 29. <https://doi.org/10.3847/1538-3881/abf8b0>
- Yamamoto, S., Nakamura, R., Matsunaga, T., Ogawa, Y., Ishihara, Y., Morota, T., et al. (2015). Global occurrence trend of high-Ca pyroxene on lunar highlands and its implications. *Journal of Geophysical Research: Planets*, 120(5), 831–848. <https://doi.org/10.1002/2014JE004740>
- Yingst, R. A., & Head, J. W. III. (1997). Volumes of lunar lava ponds in South Pole-Aitken and Orientale basins: Implications for eruption conditions, transport mechanisms, and magma source regions. *Journal of Geophysical Research*, 102(E5), 10909–10931. <https://doi.org/10.1029/97JE00717>
- Yingst, R. A., & Head, J. W. III. (1999). Geology of mare deposits in South Pole-Aitken basin as seen by Clementine UV/VIS data. *Journal of Geophysical Research*, 104(E8), 18957–18979. <https://doi.org/10.1029/1999JE000016>
- Yue, Z., Yang, M., Jia, M., Michael, G., Di, K., Gou, S., & Liu, J. (2020). Refined model age for Orientale Basin derived from zonal crater dating of its ejecta. *Icarus*, 346, 113804. <https://doi.org/10.1016/j.icarus.2020.113804>
- Zeng, X., Liu, D., Chen, Y., Zhou, Q., Ren, X., Zhang, Z., et al. (2023). Landing site of the Chang'e-6 lunar farside sample return mission from the Apollo basin. *Nature Astronomy*, 7, 1–10. <https://doi.org/10.1038/s41550-023-02038-1>
- Zhang, N., Ding, M., Zhu, M. H., Li, H., Li, H., & Yue, Z. (2022). Lunar compositional asymmetry explained by mantle overturn following the South Pole-Aitken impact. *Nature Geoscience*, 15(1), 37–41. <https://doi.org/10.1038/s41561-021-00872-4>
- Zhang, X. Y., Ouyang, Z. Y., Zhang, X. M., Chen, Y., Tang, X., Xu, A. A., et al. (2016). Study of the continuum removal method for the Moon Mineralogy Mapper (M3) and its application to mare Humorum and mare Nubium. *Research in Astronomy and Astrophysics*, 16(7), 015. <https://doi.org/10.1088/1674-4527/16/7/115>
- Zhong, S., Parmentier, E. M., & Zuber, M. T. (2000). A dynamic origin for the global asymmetry of lunar mare basalts. *Earth and Planetary Science Letters*, 177(3–4), 131–140. [https://doi.org/10.1016/S0012-821X\(00\)00041-8](https://doi.org/10.1016/S0012-821X(00)00041-8)
- Zuber, M. T., Smith, D. E., Watkins, M. M., Asmar, S. W., Konopliv, A. S., Lemoine, F. G., et al. (2013). Gravity field of the Moon from the Gravity Recovery and Interior Laboratory (GRAIL) mission. *Science*, 339(6120), 668–671. <https://doi.org/10.1126/science.1231507>